iScience

CellPress
OPEN ACCESS

Review

Magnetism of two-dimensional chromium tellurides

Jiefu Yang,[1] Chao Zhu,[1] Ya Deng,[1] Bijun Tang,[1,*] and Zheng Liu[1,2,3,*]

SUMMARY

2D ferromagnets have garnered considerable attention for their potential applications in spintronics, magnonics, and spin-orbitronics. Chromium tellurides (Cr_xTe_y), in particular, have drawn interest due to their exceptional magnetic properties and diverse range of chemical stoichiometries, attributed to the phenomenon of chromium self-intercalation. To provide an in-depth understanding of this complex material class, this review first explains the origin of 2D magnetism using two well-known 2D ferromagnets, CrI_3 and Fe_3GeTe_2, and compares the structures of $CrTe_2$, Cr_5Te_8, Cr_2Te_3, and CrTe to clarify the self-intercalation phenomenon. In addition, it summarizes the growth conditions of Cr_xTe_y using the chemical vapor deposition approach as well as commonly practiced characterization techniques for 2D ferromagnetism. This review also compares ferromagnetic properties while analyzing how Cr intercalants affect the magnetic. Finally, it suggests that more attention should be focused on this material system to unlock its full practical and academic potential, and proposes directions for future research.

INTRODUCTION

Intrinsic magnetism of two-dimensional (2D) materials has always been a heated research scope for its substantial potential in endowing additional control to the current nanoelectronics. Specifically, novel devices based on this ferromagnetic nature, such as transistors,[1–3] memory,[4,5] and spintronic-logic devices,[6] could be made even smaller provided the core ferromagnetic component is reduced into a few-layer thickness.[7–9] Ever since the ground-breaking discovery of 2D ferromagnetism in atomically thin CrI_3 and $CrGeTe_3$ in 2017,[10,11] more 2D ferromagnets candidates have been explored to pursue for the higher Curie temperature (T_C) and the enhanced stability, including but not limited to Fe_3GeTe_2,[12,13] VX_2 (X = S, Se),[14,15] and the interests of this review, chromium tellurides (Cr_xTe_y).

Cr_xTe_y has drawn tremendous interest from both academic and industrial communities for their room temperature ferromagnetism, decent chemical stability in ambient conditions, and most importantly rich structures.[16–18] The structural complexity is attributed to the stable phases formed from the chromium self-interaction of the pristine 1T-$CrTe_2$ crystals.[19] Moreover, different stoichiometries and phases can be achieved by carefully tuning the synthesis parameters using the convenient ambient pressure chemical vapor deposition (APCVD) setup.[20] The thickness dependency[19,21] and strain dependency[22–25] of Cr_xTe_y provide fascinating controllability on 2D magnetism. Moreover, intriguing magnetic behaviors, such as skyrmions,[26] biskyrmions,[27] and anomalous Hall effect,[28] have also emphasized its important role as a model platform for fundamental research. Given the complexity of composition and magnetic behaviors, it is of paramount importance to compile all reported synthesis parameters, structural information, and magnetic characterization details to eventually realize precise phase control and uncover the origin of strong ferromagnetism and its contribution from Cr intercalants.

This review endeavors to present an up-to-date overview of the research progress of Cr_xTe_y. Atomic structures of different phases are first compared to highlight their key structural differences in terms of the amount and arrangement of Cr intercalants. Next, the CVD synthesis of Cr_xTe_y is elucidated to demonstrate its potential in phase engineering. Prior to the comparison of magnetic properties, commonly used characterization methods such as the magneto-optic Kerr effect and Hall measurement are summarized and discussed. The magnetic properties of Cr_xTe_y with different compositions and phases are compared based on key indicators, T_C, and coercivity. The impact of Cr intercalants on overall spin configuration is particularly illustrated with theoretical support. Interesting phenomena, such as phase and thickness dependency, are also highlighted. In the end, the prospects for future academic research and practical application of Cr_xTe_y are proposed.

[1]School of Materials Science and Engineering, Nanyang Technological University, 50 Nanyang Avenue, Singapore 637998, Singapore

[2]CINTRA CNRS/NTU/THALES, UMI 3288, Research Techno Plaza, Singapore 637553, Singapore

[3]School of Electrical and Electronic Engineering, Nanyang Technological University, Singapore 637998, Singapore

*Correspondence: bjtang@ntu.edu.sg (B.T.), Z.Liu@ntu.edu.sg (Z.L.)

https://doi.org/10.1016/j.isci.2023.106567

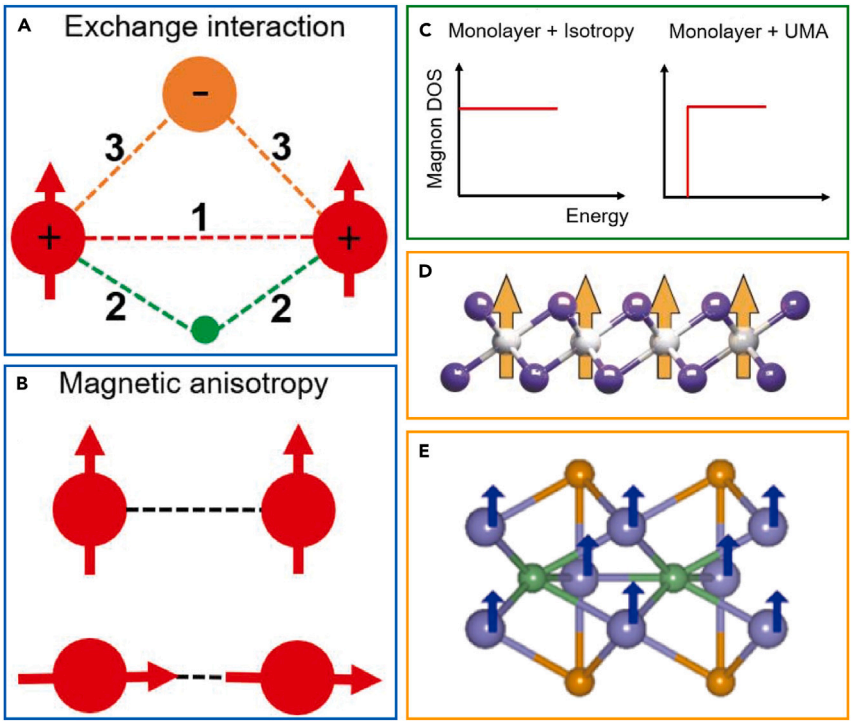

Figure 1. Reservation of ferromagnetism in the 2D limit

(A–C) (A) Three routes of the exchange interaction between neighboring spins: (1) direct exchange, (2) indirect exchange, and (3) superexchange. (B) Schematics of uniaxial magnetic anisotropy: out-of-plane magnetic anisotropy (top) and in-plane magnetic anisotropy (bottom). (C) DOS of magnons in 2D systems with different magnetic anisotropy (reproduced with permission from Gong et al.[34] Copyright 2019 American Association for the Advancement of Science).

(D) The spin configuration of CrI_3 (reproduced with permission from Huang et al.[11] Copyright 2017 Springer Nature Limited).

(E) The spin configuration of Fe_3GeTe_2 (reproduced with permission from Hu et al.[35] Copyright 2020 American Chemical Society).

ORIGIN OF 2D FERROMAGNETISM

Ferromagnetism comes from the spontaneous parallel alignment of magnetic moments in a long distance. As for 2D ferromagnetism, the history can be traced back to the 1940s, when Onsager first theoretically proposed that the long-range magnetic order can exist in a 2D Ising magnet.[29] In the past decades, some quasi-2D or thin-film magnetic systems have been reported, such as K_2NiF_4 and ultrathin Fe/Co/Ni films deposited on nonmagnetic substrates. However, K_2NiF_4 is a 3D crystal with 2D magnetic layers while the latter suffers from film discontinuity, high roughness, and low magnetization when the thickness is below 1 nm.[30] The lack of real 2D ferromagnets was changed by the realization of 2D vdW ferromagnets of monolayer CrI_3 and Fe_3GeTe_2. To elaborate on how ferromagnetic ordering is reserved in two dimensions for these materials, concepts of the exchange interaction and magnetic anisotropy are necessarily explained as follows.

The exchange interaction, arising from quantum mechanics, determines the alignment of neighboring magnetic moments, i.e., spins in neighboring atoms.[31] The exchange interaction results from the Coulomb interaction between electrons and the Pauli exclusion principle,[32,33] which states that the wavefunction of electrons must be antisymmetric. If the exchange coupling constant is positive, spins tend to be parallel. While if the exchange coupling constant is negative, spins tend to be antiparallel. The exchange interaction between spins can be established in several ways (Figure 1A). Red dashed line 1 represents direct exchange when electron orbitals of adjacent atoms have great overlapping. Green dashed line 2 with a green ball representing an electron demonstrates indirect exchange, common in metals, when spin alignment is mediated by the conduction electrons. And orange dashed line 3 with an orange ball representing an ion demonstrates a superexchange when spins are mediated by a mutual neighbor.[34] Exchange interaction

alone cannot address the reservation of ferromagnetic ordering in a 2D system since it is only accounted for the interplay of adjacent magnetic moments. In order to preserve long-range magnetic order in 2D materials, magnetic anisotropy is a prerequisite.

Magnetic anisotropy refers to the preferred orientation of overall spin alignment. The simplest cases are uniaxial magnetic anisotropy in the out-of-plane direction or one of the planar directions (Figure 1B). The overall magnetic anisotropy of a material system is a concerted result of several contributing factors including but not limited to magnetocrystalline anisotropy,[36] exchange anisotropy,[37] shape anisotropy,[38] and magnetoelastic anisotropy.[39] Being Bosonic, magnons are thermal excitations that lead to the decrease of magnetization below T_C.[40] For isotropic 2D magnets, there is no magnon excitation gap (left panel in Figure 1C). When the temperature is nonzero, a massive amount of magnons will be generated by the thermal energy, leading to the destruction of long-range order, as stated by the Mermin-Wagner theorem. However, if magnetic anisotropy is introduced, an obvious gap in magnon DOS would be opened at sufficiently low system energy, indicating the inhibition of thermal excitation and thus the stabilization of the ferromagnetic (FM) ordering.[34] Notably, the temperature at which ferromagnetic ordering starts to manifest is commonly known as the T_C, which can be inferred from the sharp elevation of DOS since the system energy is positively related to the system temperature.

To illuminate the impact of magnetic anisotropy on the overall ferromagnetism, side views of both monolayer CrI_3 and Fe_3GeTe_2 structures are demonstrated. Ferromagnetic monolayer CrI_3 has a typical out-of-plane easy axis with a T_C of 45 K and a coercivity of about 50 mT under 15 K.[39] A plane of chromium (Cr) ions in white color are sandwiched by two planes of iodine (I) ions in purple (Figure 1D). Each Cr ion is surrounded by six I ions, arranged in an octahedral ligand configuration. It is known that the single ion magnetic anisotropy stems from the interaction of spin-orbit coupling and the crystal field and its strength generally follows λ^2/Δ where λ denotes magnetic ion atomic spin-orbit coupling and Δ denotes energy splitting in the t_{2g} triplet in octahedron configuration.[41] Since the energy difference in the t_{2g} triplet is an order greater than the energy arising from the ion atomic spin-orbit coupling, the single ion magnetic anisotropy is substantially suppressed.[41] As such, the Ising model with single-spin-flip dynamics cannot effectively address the ferromagnetism origin of the CrI_3 materials system. On the other hand, in the octahedral environment given by the structure, the angle of the Cr-I-Cr bond is close to the ideal 90°, therefore favoring the ferromagnetic Cr-Cr coupling with a preferred out-of-plane spin alignment (Figure 1D) through a superexchange interaction mediated by the mutual I ion according to the Goodenough-Kanamori-Anderson guidelines.[42,43] As for monolayer Fe_3GeTe_2, the magnetocrystalline anisotropy caused by spin-orbit coupling plays a dominating role in endowing the monolayer FGT ferromagnetism with a high T_C of 130 K and a large coercivity of about 75 mT under 80 K condition.[12] Fe atoms are arranged in three middle sublayers, sandwiched by two sublayers of Te atoms (Figure 1E). Due to the symmetric positions of top and bottom Fe sublayers resulting in the cancellation of the spin-orbit coupling effect, the magnetocrystalline anisotropy is solely contributed by the central layer, giving rise to an easy axis of spins perpendicular to the basal plane.[44] The origin of the ferromagnetism in Cr_xTe_y mainly comes from the ferromagnetic coupling via a superexchange interaction of Cr-Te-Cr in the backbone 1T-$CrTe_2$.[45] However, the additional chromium atoms in between planes must also contribute to the overall spins since Cr atoms are ferromagnetic in nature. Therefore, understanding how Cr intercalants are arranged in between layers and knowing the structural differences might be beneficial in exploring the discrepancies in magnetic properties.

COMPARISON OF ATOMIC STRUCTURE ACROSS PHASES

A holistic structural comparison is discussed based on the simulated structures and measured data to elaborate on the similarities and differences of 5 characteristic compositions, $CrTe_2$, tr-Cr_5Te_8, Cr_2Te_3, Cr_3Te_4, and CrTe, in an order of increasing Cr intercalants (Figure 2). Due to different symmetrical conditions stemming from various unit cell or space groups, the above structures are viewed along the planes equivalent to the ab, bc, and ac planes of 1T-$CrTe_2$, respectively. As the primitive structure, 1T-$CrTe_2$ has no interlayer Cr contents and shows a typical AbC intralayer stacking order of Te-Cr-Te atomic planes, indicating the local octahedral arrangement around each Cr atom, which is exemplified by the structure of 1T MoS_2 (Figure 2A).[46] 1T-$CrTe_2$ belongs to the space group *P-3m1* with lattice parameters a = 3.77 Å and c = 6.01 Å[47] and shows an interlayer AA stacking pattern with an interlayer distance of 2.97 Å.[21] Both the absence of primary bonds and considerably wide interlayer distance confirm van der Waal's interaction between the repeating units, revealing its layered nature.

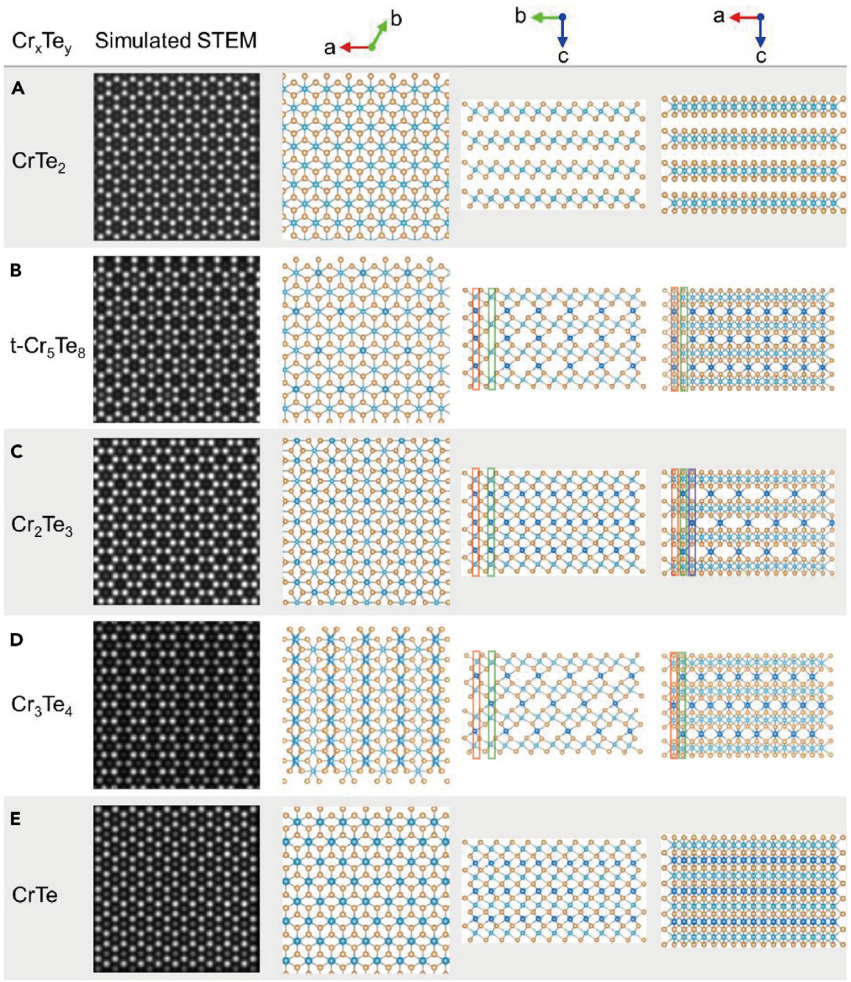

Figure 2. Structural comparison of Cr_xTe_y

(A–E) Simulated STEM images and corresponding atomic structures of (A) $CrTe_2$, (B) trigonal Cr_5Te_8, (C) Cr_2Te_3, (D) Cr_3Te_4, and (E) CrTe viewed along ab, bc, and ac planes (reproduced with permission from Chen et al.[19] Copyright 2021 John Wiley & Sons, Inc)

Starting from the basic structure of 1T-$CrTe_2$, other structures of the Cr_xTe_y series can be considered the result of the Cr self-intercalation of the $CrTe_2$ backbones. Taking CrTe as an extreme example, an additional Cr layer, colored in darker blue, is inserted in between every two neighboring $CrTe_2$ layers (Figure 2E). CVD-grown CrTe crystals adopt the hexagonal NiAs structure, which belongs to the space group of $P6_3/mmc$ with lattice parameters a = 3.98 Å and c = 6.23 Å.[48] Since the unit cell of NiAs-type CrTe encloses three Cr layers and two Te layers,[17] the equivalent interlayer distance between two $CrTe_2$ backbones is roughly estimated to be 3.12 Å, showing only a slight elongation even with the insertion of a whole Cr layer. After mentioning the two extremes, other compositions, in the same analogy, can be viewed as 1T $CrTe_2$ backbones with incomplete occupancy of Cr intercalants. For example, the atomic structure of Cr_5Te_8 could be perceived as 1T-$CrTe_2$ with 25% occupancy of Cr intercalants (Figure 2B). Depending on the specific arrangement, structures of Cr_5Te_8 could be further classified into tr-Cr_5Te_8 and m-Cr_5Te_8, in which the prefixes are coined based on their crystal systems of trigonal or monoclinic, respectively. tr-Cr_5Te_8 belongs to *P-3m1* space group with calculated lattice constants to be a = 7.90 Å and c = 6.03 Å while m-Cr_5Te_8 belongs to *C2/m* space group with lattice parameters a = 7.89 Å, b = 9.12 Å, and c = 12.26 Å.[19,28] Likewise, Cr_2Te_3 could be viewed as the 33.3% filling of sites in intercalating positions (Figure 2C). A characteristic Cr_2Te_3 structure belongs to *P-31c* space group with lattice parameters a = 6.81 Å and c = 12.1 Å.[49] Similarly, the atomic structure of Cr_3Te_4 is analogous to 1T-$CrTe_2$ with 50% intercalated sites evenly filled by Cr atoms (Figure 2D). Cr_3Te_4 belongs to space group *P2/m*

and the lattice parameters are a = 7.69 Å, b = 3.85 Å, and c = 6.17 Å.[27] The positions of Cr intercalants in different phases are indicated by boxes in different colors. For example, in the bc planes, orange and green boxes represent two sets of equivalent positions. Different phases thus could be conveniently identified provided cross-sectional HAADF-STEM images are collected. Remarkably, in the ac plane of Cr_2Te_3, the filling of Cr intercalants adopts a periodicity of three, highlighted by boxes of three colors, unlike the periodicity of two observed in cases of tr-Cr_5Te_8 and Cr_3Te_4.

The insertion of the Cr layer and varying filling conditions intuitively affect the structure. The most pronounced impact is the interlayer distance. Using the same approach for estimating the interlayer distance in CrTe, interlayer distances in tr-Cr_5Te_8, Cr_2Te_3, and Cr_3Te_4 are calculated to be 3.02, 3.03, and 3.09 Å, respectively. When interlayer distances or interlayer distances equivalences are compared, it could be seen that adjacent 1T-$CrTe_2$ layers are kept monotonically further with more Cr intercalants. A similar finding was reported by Bian, who calculated that the spacing between the monolayer Cr_xTe_y and the substrate monolayer WSe_2 keeps increasing with a greater amount of Cr intercalants in the commensurate Cr_xTe_y/WSe_2 structure.[50] Another impact would be the distortion of a local structure due to the introduction of covalent bonds. The incomplete filling of intercalating layers causes discrepancies in the coordination conditions of Te atoms. Te atoms connected to Cr intercalants are pulled by the additional atom, thus shortening the interlayer distances, and causing an undulating configuration.[28,51]

PREPARATION OF Cr_xTe_y BY CVD

Many synthesis techniques, such as molecular beam epitaxy and pulsed laser deposition (PLD), have been reported to achieve epitaxial growth of Cr_xTe_y with various stoichiometries and phases.[16,52–57] However, the APCVD technique is predominantly utilized for its relatively simple setup and desired quality of final products in terms of great crystallinity, uniform composition, and ultrathin thickness.[20,58–60] The synthesis of ultrathin chromium tellurides, including van der Waals 1T-$CrTe_2$ and nonlayered Cr_2Te_3, Cr_3Te_4, Cr_5Te_8, and CrTe, using the CVD approach has been frequently reported in the past decade. For the preparation of 2D transition metal dichalcogenides (TMDCs), the strengths of the CVD approach mainly lay on the desirable quality of final products. The typical setup for Cr_xTe_y synthesis is an APCVD system with accurate control of temperature, carrier gas types, and flow rates (Figure 3A). Other than these conventional synthesis parameters, types of precursors and substrates, substrate layouts, and even cooling conditions are considered essential in preparing various phases of Cr_xTe_y nanoflakes (Table 1).

The common CVD procedure is described in detail to highlight the importance of those parameters. First, the chalcogen source and transition metal (TM) precursor are placed on separate ceramic or quartz boats at different locations to enable separate temperature control. All recipes use tellurium powder as the chalcogen source. However, choices for TM precursors are much richer, including chromium powder, chromium chlorides, and a combination of them. Notably, sodium chloride is commonly introduced into the TM precursors as a melting agent.[60] Choices of precursors often place an effect on either the composition of the final product or the temperature window of reaction as suggested by the listed growth parameters, as supported by the recipes in Table 1. As for the substrate, it could be placed in the same boat with the TM precursor or on a third boat downstream with various layouts. They could be facing upward, upside down, upside down but tilted, or stacked to attain a space-confined manner.[63] Before the heating, the quartz tube is first flushed with a high volume of inert gas for endured time to expel the residue moisture and oxygen inside the tube, to endure the good quality of final products. Next, carrier gases are adjusted accordingly and maintained. The system is finally ready for the following heating, dwelling, and cooling processes with designated duration, respectively. Typically, the temperatures, at which the chalcogen source and TM precursors are located, are decided by their relevant vapor pressures of the specific temperatures while the temperature of the substrate is mainly determined by the activation energy of the reaction and deposition rate of the final product.[64–68] Normally, larger samples can be obtained after prolonged growth duration, but the thickness might also increase during the course as the crystal growth is not perfectly epitaxial and thus nucleation on the existing layers is unavoidable.[48,69] Remarkably, other than the growth time, both the ramping duration and cooling duration place a significant influence on the composition of the final product since nucleation and growth of nanoflakes occur over a considerably wide temperature range, and phase freezing or transformation may also occur during the cooling step.[28]

The current progress of the CVD-grown 2D CrTe, Cr_2Te_3, Cr_5Te_8, and $CrTe_2$ nanoflakes has been demonstrated by the optical microscopic and atomic force microscopic images (Figures 3B–3J). Wang et al.

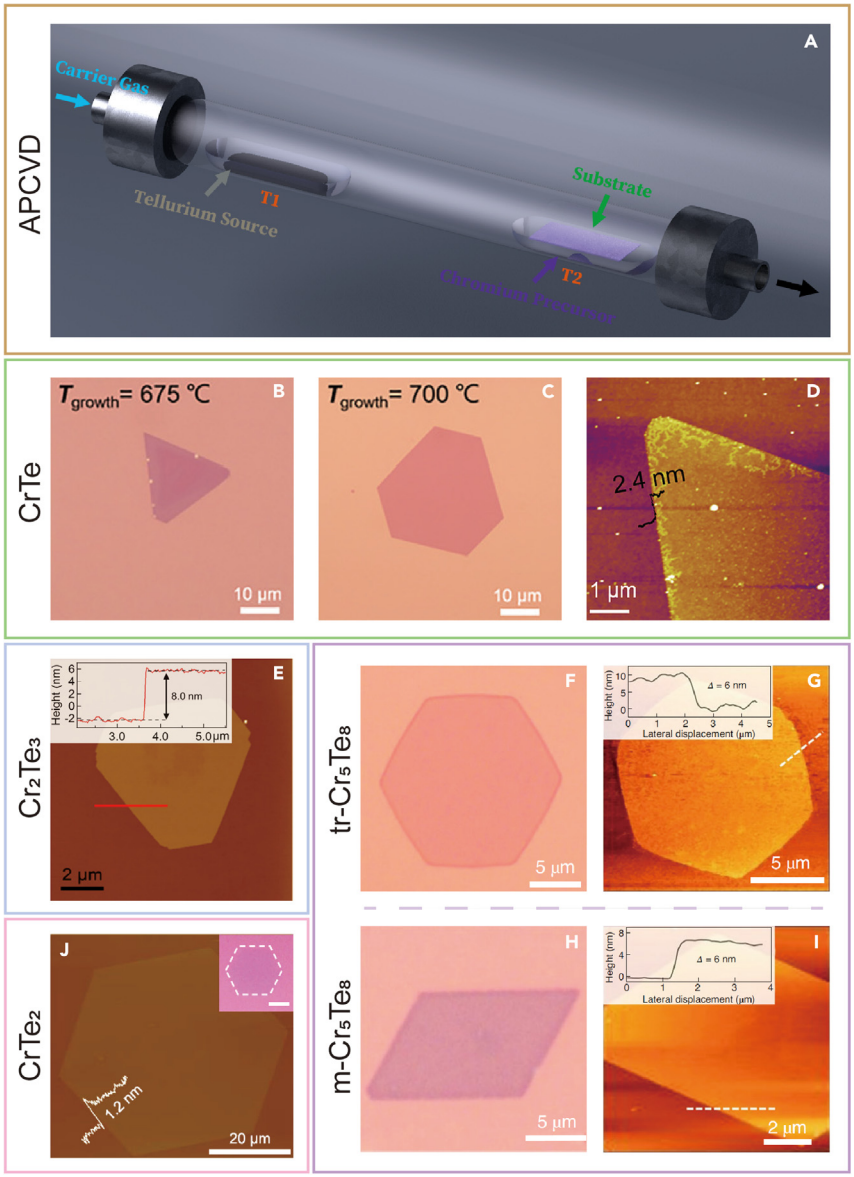

Figure 3. Chemical vapor deposition setup and overview of CVD-prepared 2D Cr_xTe_y

(A) The schematic of a typical CVD setup for Cr_xTe_y synthesis with controlled parameters marked by different colors.

(B–D) A sample CrTe nanoflake: the optical images of CrTe obtained at growth temperatures of (B) 675°C and (C) 700°C. (D) The AFM image of a sample nanoflake (reproduced with permission from Wang et al.[48] Copyright 2020 Royal Society of Chemistry).

(E) The AFM image of the Cr_2Te_3 nanoflake (reproduced with permission from Coughlin et al.[61] Copyright 2020 American Chemical Society).

(F–I) Samples of Cr_5Te_8 nanoflakes in two phases: (F) The optical and (G) AFM images of trigonal Cr_5Te_8. (H) The optical and (I) AFM images of monoclinic Cr_5Te_8 (reproduced with permission from Tang et al.[28] Copyright 2022 Springer Nature Limited).

(J) The AFM image of $CrTe_2$ (reproduced with permission from Meng et al.[47] Copyright 2021 Springer Nature Limited).

synthesized ultrathin nonlayered CrTe nanoflakes with thicknesses down to 2.4 nm on SiO_2/Si substrate (Figure 3D).[70] The synthesized CrTe nanoflakes normally take triangular or hexagonal shapes macroscopically (Figures 3B and 3C). Furthermore, the correlation between the thickness of the synthesized sample and the growth temperature was reported. By raising the temperature from 675°C to 750°C while maintaining other growth parameters, CrTe nanoflakes with gradually increasing thickness could be

Table 1. Synthesis parameters, structural information, and magnetism overview of CVD-prepared Cr_xTe_y

Composition	Transition metal precursor	Substrate	Carrier gas [flow rate (sccm)]	Growth temperature (°C)	Growth time (min)	Modification	Phase	Space group	Lattice parameters (Å)	Magnetic types	Probing techniques	Reference
CrTe	$CrCl_3$, NaCl	SiO_2/Si	Ar [100]; H_2[10]	675–750	3	–	Hexagonal	$P6_3/mmc$	a[3.98]; c[6.23]	Ferromagnetic	MOKE, RMCD	Wang et al.[48]
CrTe	Cr, $CrCl_3$, NaCl	SiO_2/Si	Ar [100]; H_2[5]	700	5	–	Hexagonal	$P6_3/mmc$	–	–	–	Guo et al.[62]
Cr_3Te_4	$CrCl_3$	SiO_2/Si	Ar [40]; H_2[15]	670–710	5	–	Monoclinic	P2/m	a[7.69]; b[3.85]; c[6.17]	Ferromagnetic	RMCD, VSM, transport	Li et al.[27]
Cr_2Te_3	$CrCl_3$, NaCl	Mica	Ar [200]; H_2[50]	650	5	Stacked substrates	Trigonal	P-31c	a[6.8]; c[12.1]	Ferromagnetic	VSM, MOKE	Bian et al.[49]
Cr_2Te_3	$CrCl_3$	SiO_2/Si	Ar [25]	750	0	Slow ramping	Trigonal	P-31c	a[6.8]; c[12.1]	Ferromagnetic	MOKE	Coughlin et al.[61]
Cr_2Te_3	$CrCl_3$, NaCl	Mica	Ar+H_2 [total 150]	850	–	–	–	–	–	Ferromagnetic	Transport	Wen et al.[51]
Cr_5Te_8	$CrCl_2$	SiO_2/Si	Ar [50]; H_2[20]	600–900	10	Tube-in-tube	Trigonal	P-3m1	a[7.9]; c[6.04]	Ferromagnetic	MOKE	Chen et al.[19]
Cr_5Te_8	$CrCl_3$	Monolayer WSe_2/ sapphire	Ar [90]; H_2[10]	600	10	–	Trigonal	–	a[6.72]; c[11.6]	Ferromagnetic	RMCD	Bian et al.[50]
tr-Cr_5Te_8	$CrCl_3$	SiO_2/Si	Ar [100]; H_2[5]	670–730	2	Slow cooling	Trigonal	P-3m1	a[7.99]; c[5.87]	Ferromagnetic	RMCD	Tang et al.[28]
m-Cr_5Te_8	$CrCl_3$	SiO_2/Si	Ar [100]; H_2[5]	670–730	2	Fast cooling	Monoclinic	C2/m	a[7.89]; b[9.12]; c[12.26]	Ferromagnetic	RMCD	Tang et al.[28]
$CrTe_2$	$CrCl_2$	SiO_2/Si	Ar [200]; H_2[1]	709.85 (983 K)	2	–	Trigonal	P-3m1	a[3.77]; c[6.01]	Ferromagnetic	RMCD, transport	Meng et al.[47]

prepared.[48] Coughlin has synthesized single-crystalline Cr_2Te_3 nanoflakes with thickness down to 8 nm, equivalent to about 7-unit cells, on SiO_2/Si substrates (Figure 3E).[61] Notably, since this work employed a three-boat setup in which the substrate quartz boat was placed downstream to the precursor boat, the thickness of the nanoflakes could be lowered if the distance between the two boats increases.[61] The synthesis of single unit-cell thick Cr_2Te_3 nanoflakes on mica substrates has also been reported in the works of Bian[49] and Wen,[51] respectively. Cr_5Te_8 nanoflakes of both trigonal and monoclinic phases are prepared by Tang and the thicknesses can reach as low as 6 nm while maintaining smooth surface finishes, as evidenced by the atomic force microscope (AFM) line profiles in insets[28] (Figures 3F–3I). This work stresses that phase selectivity is realized by controlling growth temperature and cooling rate. Supported by the calculated energy difference between the two phases, a higher growth temperature thermodynamically favors the formation of tr-Cr_5Te_8. On the other hand, fast cooling is conducive to the formation of the distorted m-Cr_5Te_8 phase. In addition, C. Chen synthesized trigonal Cr_5Te_8 of thickness down to 1.2 nm via a customized tube-in-tube CVD setup, in which a tube of smaller diameter, with one opening facing upstream and another being a pinhole facing downstream, accommodates the chalcogen, precursor crucibles, and the substrate mica in the following order.[19] The difference in pore sizes at two ends of the quartz tube creates a Te-rich environment inside the smaller tube, thus favoring the formation of Cr_5Te_8. Similarly, Bian also adjusted the conventional CVD method to promote the formation of Cr_5Te_8 by substituting common substrates with monolayer WSe_2.[50] This work highlights the interfacial dative bond formation between monolayer WSe_2 and Cr_5Te_8 is the key to stabilizing the metastable phase and boosting the epitaxy growth of the covalent Cr_5Te_8 crystals. Lastly, Meng et al. synthesized 1T-$CrTe_2$ nanoflakes with thickness down to 1.2 nm, which is equivalent to 2-unit cell thickness, as demonstrated by the AFM image (Figure 3J).[47] Compared to the mechanical exfoliation of bulk 1T-$CrTe_2$ crystal, CVD synthesis tends to yield products with uniform thickness and larger sizes, which benefits subsequent device fabrication and characterization. Ultrathin Cr_3Te_4 nanoflakes are also reported to be synthesizable by the CVD method and the detailed parameters are archived in Table 1.[27] Besides the CVD method highlighted in this work, another thin-film deposition method, the PLD technique is also capable of epitaxially growing the above-mentioned 2D Cr_xTe_y.[55,71] Moreover, a new composition, Cr_4Te_5 has been prepared on Al_2O_3 (0001) substrates using this technique.[52–54]

MAGNETIC CHARACTERIZATION OF 2D MATERIALS

Due to their small loading and minuscule size, 2D magnets including chromium tellurides require demanding methods for accurate measurement to avoid interference from the environment and testing equipment itself. The general approach to studying magnetic-dependent properties is to subject the sample to an external magnetic field below the T_C and collect relevant signals based on different working principles while varying the magnetic field and temperature accordingly. The processed signal, such as current, voltage, and light polarization, would be collected under different field and temperature conditions and eventually plotted as a function of external field strengths. When the sample manifests ferromagnetism, normally a signature hysteresis loop could be perceived on plots, indicating that the ferromagnetic ordering of the sample preserves with certain remanence and coercivity. Also, with the temperature-dependent hysteresis loop, the T_C could be estimated. Moreover, saturation magnetization could be measured if the system is first calibrated using a sample with a known saturation value. Including methods listed in Table 1, all commonly practiced techniques could be categorized into optical techniques, electrical techniques, and direct measurement based on Faraday's law of induction. In the remaining part of the section, all these methods would be introduced, and briefly evaluated in the end.

Optical approaches are convenient due to their non-contact nature, high sensitivity, and fine resolution.[72] Two state-of-art approaches are based on the magneto-optic Kerr effect (MOKE, also known as magnetic circular birefringence) and magnetic circular dichroism (MCD), respectively. Both setups use a near-normal incident light, i.e. 4° in K. Sato's setup to interact with the flat surface of the target 2D magnets and collect the reflective lights with changes on their complex optical conductivities, caused by magneto-optic effects (Figures 4A and 4B).[73] For MOKE, the incident light used is a linearly polarized light (LPL) with known polarization and the change in the imaginary part of the complex optical conductivity is analyzed.[63] The right-circularly polarized component (RCP) and left-circularly polarized component (LCP) resolved from the linearly polarized light experience different phase shifts due to different refractive indices, thus resulting in a rotation of polarization plane, i.e., Kerr rotation (Figure 4A).[73] However, the intensity of the light remains unchanged as indicated by the equal lengths of the incident and reflective LPL. A facile design to roughly estimate the Kerr rotation is to insert a linear polarizer, with a polarization plane perpendicular to that of the

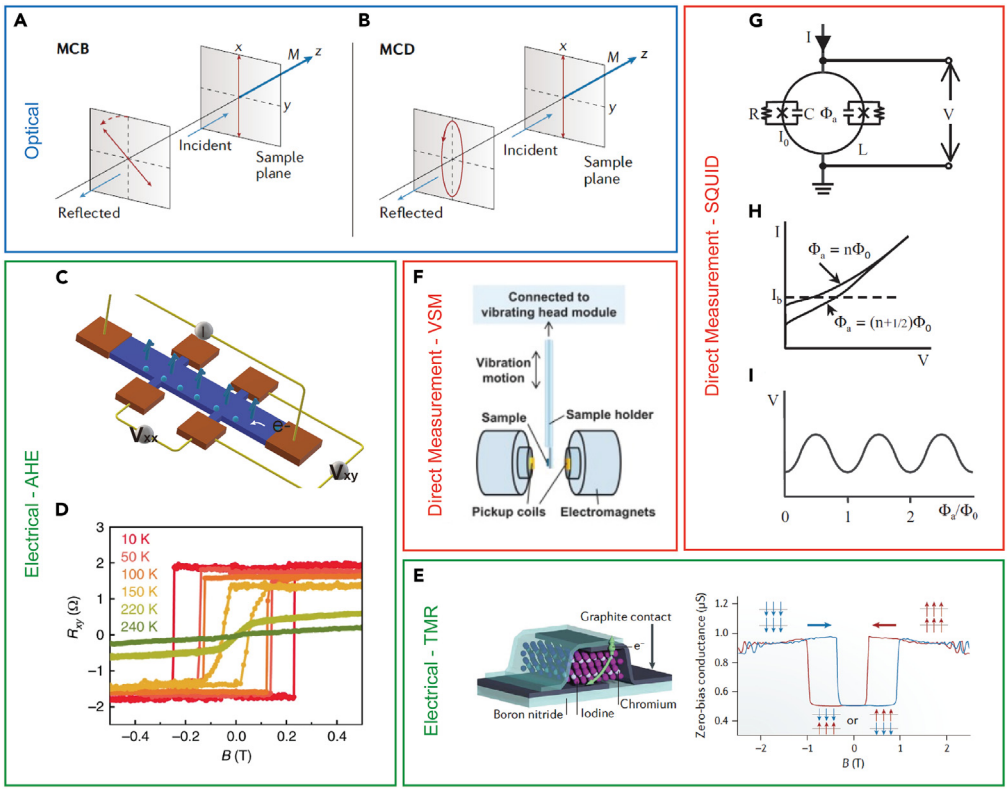

Figure 4. Characterization methods for out-of-plane magnetism in 2D materials (A, B) The optical approaches

(A–C) Schematics of magnetic circular birefringence, also known as magneto-optical Kerr effect, and (B) magnetic circular dichroism (reproduced with permission from Mak et al.[72] Copyright 2019 Springer Nature Limited) (C) The schematic of a Hall bar device.

(D–G) A plot of Hall resistance against external field strength displaying hysteresis loops to demonstrate anomalous Hall effect. (reproduced with permission from Kang et al.[70] Copyright 2020 Springer Nature Limited) (E) The magnetic tunnel device and a plot of zero-bias conductance against external field strength to elaborate the tunnel magnetoresistance phenomenon (reproduced with permission from Klein et al.[75] Copyright 2018 American Association for the Advancement of Science) (F) The schematic of the vibrating sample magnetometer (reproduced with permission from Adeyeye et al.[76] Copyright 2015 Elsevier B.V.) (G-I) An overview of superconducting quantum interference device: (G) The schematic of SQUID.

(H) The determination of maximal and minimal voltage at defined bias current.

(I) A plot of voltage against oscillating flux to explain how to sample magnetization is extracted from oscillating voltage signals (reproduced with permission from Braginski[77] Copyright 2004 Wiley-VCH Verlag GmbH & Co. KGaA).

initial LPL, on the reflective path to isolate the rotated component and measure its intensity using a photodetector since the intensity of the rotated portion is directly proportional to the sample's magnetization.[74] On the other hand, MCD is another type of magneto-optic interaction that causes different absorption of RCP and LCP, namely the real part of the complex optical conductivities, therefore changing the ellipticity of the incident light (Figure 4B).[73] A state-of-art approach uses alternating RCP and LCP of equal intensity as the incident light and estimates the magnetization of the target material by collecting the absorption differences in RCP and LCP. Notably, K. Sato designed a single setup based on a piezo-birefringent modulator to realize easy switching of MOKE and MCD while achieving a high sensitivity (0.002° for Kerr rotation) and a fine detection resolution of 12 nm.[73]

Other than optical approaches, electrical methods, such as the electrical transport technique based on the Hall effect and electronic tunneling transport technique, are also utilized to explore the magnetic states of 2D materials. Although they commonly involve complicated procedures for device designing and preparation, the electrical approaches are more versatile for their expanded capacity to identify antiferromagnetism and more convincing since they measure the performance of the whole material.[78] In a typical

Hall bar device for magneto-transport measurement (Figure 4C), a potential difference is applied across the long ends. When the device is subject to a magnetic field, charges will be accumulated and finally form the Hall voltage in the transverse direction. By measuring the Hall voltage (V_y), the transverse Hall resistivity can be derived from the formula $\rho_{xy} = V_y\, t/I_x$, in which t is the sample thickness and I_x is the current along the x axis. Since the Hall resistivity is proportional to the overall magnetization of the sample system, a hallmark hysteresis loop in a plot of Hall resistivity against external magnetic field strength is expected for an intrinsic ferromagnetic material. The ρ_{xy}-H plots for 2D FeTe nanoflakes at various temperatures show that the coercive field can be nonzero up to 220 K, both indicating their ferromagnetic nature and estimating their T_C (Figure 4D).[70] Notably, Hall resistivity for a ferromagnetic material consists of two parts: the ordinary portion stemming from the external magnetic field and an additional contribution arising from the intrinsic magnetism of the material, which is called the anomalous Hall effect (AHE).[79] Remarkably, magnetotransport measurement has also been performed to identify noncollinear antiferromagnetic (AFM) materials such as Mn_5Si_3[79] and Mn_3Ge[80,81] as intrinsic AHE is nonzero for noncollinear antiferromagnets and its contribution could be extracted from the plot of Hall resistivity as a function of external magnetic field strength. Moreover, by aligning the external magnetic field direction to the planar directions of 2D materials, the in-plane ferromagnetism of 2D materials or heterostructures can be also detected if AHE persists.[82] Another innovative method to identify ferromagnetism is done via anisotropic magnetoresistance (AMR), which refers to the dependence of electrical conductivity of material on the magnetization direction and is believed to originate from the concerted effects of spin-orbit interaction and the asymmetric arrangement of the ferromagnetically ordered states, which engenders discrepancies in the scattering of the electrons depending on the magnetization direction.[83,84] Negative MR is typically found in ferromagnets along the easy axis of spins.[85] Recent studies on 2D CrI_3 have also demonstrated the capability of AMR in probing the A-type AFM in a material,[86,87] where the spins in the same plane are of the same direction while the spins in adjacent planes are oppositely aligned, giving zero net spin moments when the layer number is even.[88] For example, in a double-layered CrI_3 tunnel junction constructed by Song's group (Figure 4E), the conductivity in the out-of-plane direction experienced a plateau regime at low magnetic fields but a significant enhancement at high fields. The abrupt transitions suggest the instant flipping of spins and the hysteresis features reflect the hindrance of the spin-flip transition, indicating the ferromagnetic ordering in each plane. AMR in planar direction is also handy to probe in-plane ferromagnetism, but to our best knowledge, no relevant works on true 2D materials have ever been reported although it is a commonly used approach used for thin films of ferromagnetic alloys.[89]

Governed by Faraday's law of induction, which states that an electromotive force (e.m.f.) would be induced in a closed loop subject to changing magnetic field, i.e., magnetic flux, direct measurement of magnetization could be achieved via either vibrating sample magnetometer (VSM) or superconducting quantum interference device (SQUID) magnetometer.[90] For VSM, a tested sample is loaded onto a holder connected to a rod vibrating in a vertical motion, and subject to an external magnetic field in the direction perpendicular to the vibration (Figure 4F). If the loaded sample is ferromagnetic, the moving sample emanates magnetic flux, thus inducing e.m.f. and then current in the pick-up coil. Since the magnetization is directly proportional to the induced current, absolute measurement of the magnetic moment could be obtained through comparison with a calibration sample with known magnetization.[90] Identical to previously mentioned techniques, procedures of changing the applied external magnetic field to obtain hysteresis and varying the ambient temperature to estimate the T_C are routinely practiced. Also, a direct measurement approach, the SQUID magnetometer provides a much better sensitivity (<0.1 μemu) in reading magnetic moments as compared to VSM due to its special design of detector rather than the simple pick-up coils.[91] The detector of a direct-current SQUID consists of two Josephson junctions connected in parallel (Figure 4G). When in use, a bias current is applied across two ends and the magnetic flux penetrating in the planar direction induces continuously changing potential differences owing to the Meissner effect[92] and Josephson effect.[92–94] In practice, a bias current is applied to a DC SQUID to drive Cooper pairs in superconducting material in the Josephson junction to tunnel through the insulator in between the two superconductors. Since any magnetic flux applied to the ring would induce a looping current ($I_{Loop} = \Phi_{Loop}/L_{Loop}$), the quantum-mechanical phase changes across each junction are altered in a different manner depending on the direction of the circulating current induced in the loop.[95] Consequently, the critical current, which governs the current passage, of each junction is changed, therefore resulting in an oscillating potential (Figure 4I). Potential difference reaches its maximum when there is no external field or the flux administered to the SQUID ring equals an integral number of flux quanta while reaches a minimum when the flux administered equals a half-integral number of quanta.[96] At a specific bias current indicated by the dashed

Table 2. Comparison of the magnetic characterization methods for 2D materials

Methods	Principle	Advantages	Disadvantages
Magneto-optical approach	MOKE, MCD	Non-contact nature; High sensitivity; High resolution	Requiring careful calibration; Limited testing domain
Electrical transport	AHE	High sensitivity; Evaluating the overall performance; Wide range of temperature capability	Requiring device fabrication
Tunneling transport	AMR	–	Requiring device fabrication; Limited application
VSM	Faraday's law of inductions	Direct Measurement; Wide range of temperature capability	Easily affected by the holder; Size requirement of the sample (micrometer)
SQUID	Faraday's law of inductions, Meissner effect, Josephson effect	Direct Measurement; High sensitivity	The size requirement of the sample (micrometer)

line in plots of current as a function of voltage for both scenarios (Figure 4H), the exact maximal and minimal values can be inferred. The SQUID approach thus realizes an accurate measurement of tiny flux change through a more convenient reading of voltage change.

Table 2 summarizes the working principle and provides a brief evaluation of the above-mentioned characterization from the practical perspective.[72,75,90] Since each technique has its strengths and shortcomings, multiple techniques were conventionally used to accurately explore the magnetism in Cr_xTe_y, as evidenced by Table 1. In practice, preliminary confirmation of the existence of ferromagnetic spin order in the sample is done by non-contact optical or VSM for the great convenience endowed by their non-contact feature. However, neither method is capable of accurately characterizing the magnetic properties alone since optical approaches only probe magnetism in a small domain limited by the spot size and VSM has undesirable sensitivity due to the relatively small loading amount of 2D material as compared to the holder. Besides, magnetic contaminations on the substrate are very likely to influence the validity of the measurement. The electrical transport method, which requires arduous pre-testing preparation, is thus commonly carried out to accurately measure the overall magnetic properties of the sample and exclude influences from magnetic contaminations.

MAGNETIC PROPERTIES OF Cr_xTe_y

Table 3 summarizes the key magnetic properties of various CVD-grown Cr_xTe_y, T_C, and the coercive force, from previously reported literature. For each recorded sample, its thickness is specifically stated since thickness has a significant influence on the magnetic properties of low-dimensional materials. And for each composition, only samples with the lowest thickness and/or a thickness close to 10 nm are archived in the consideration of being qualified for 2D materials and valid comparison. Due to the limited data, no conclusive relation between composition and magnetic properties could be established for all Cr_xTe_y phases. Nonetheless, a few facile trends would be extracted from the data available. Juxtaposing the T_c of CrTe, Cr_2Te_3, and $CrTe_2$ prepared on the same substrate SiO_2/Si with comparable thicknesses of 11, 11.2, and 10 nm accordingly, it could be observed that PM-FM transition happens at a higher temperature for the sample with fewer Cr intercalants, which facially suggests that lower Cr contents endow greater resistance to thermal perturbation. However, this trend is confronted by most of the currently available analyses stating that the increasing Cr intercalants would enhance the ferromagnetic exchange interaction, and hence lead to increased T_C.[57,97] As for coercive field strengths, a positive correlation with Cr intercalants can also be extracted from the data comparison of CrTe, Cr_3Te_4, and Cr_5Te_8 with close thicknesses of 11, 10.7, and 10 nm, presuming coercivity does not vary considerably at a temperature range between 10 K and 50 K. It indicates that the added Cr atoms in the intercalation sites pose an additional hindrance to the spin flipping, which is also contradicted by past observations of higher Cr intercalants promoting in-plane spin alignment, therefore leading to the magnetic isotropization and reduced coercive field in the c-direction due to the depinning process.[57] However, a clear aberration to this trend comes from 10-nm-thick $CrTe_2$, showing a substantially high coercivity of about 0.85 T at 2 K and about 0.35 T at 60 K. It suggests the complexity of the impact of Cr intercalants on the overall magnetic performances of the system.

Intuitively, the Cr intercalants introduce extra spins into the system, therefore enhancing the saturation magnetization regardless of the spin directions. Moreover, these additional spins would also place great

Table 3. Magnetic properties of CVD-grown Cr_xTe_y

Composition	Substrate	Thickness (nm)	T_C (K)	Coercive field strength (T) and temperature (K)	Reference
CrTe	SiO_2/Si	11[a]	140	0.4 (10)	Wang et al.[48]
Cr_3Te_4	SiO_2/Si	3.3	165	N.A.	Li et al.[27]
		10.7[a]	N.A.	0.3 (10)	
Cr_2Te_3	Mica	5.5	280	0.2 (30)	Wen et al.[51]
		11.2[a]	180	N.A.	
	SiO_2/Si	13.9	195	0.03 (170)	Coughlin et al.[61]
Cr_5Te_8	Monolayer	8.4	N.A.	0.7 (5)	Bian et al.[50]
	WSe_2/Sapphire	4.5	N.A.	0.4 (5)	
	SiO_2/Si	6 (trigonal)	125	0.01 (100)	Tang et al.[28]
		6 (monoclinic)	150	0.1 (100)	
	SiO_2/Si	15	130	N.A.	Chen et al.[19]
		10[a]	N.A.	0.2 (50)	
$CrTe_2$	SiO_2/Si	3.0	189	0.46 (100)	Meng et al.[47]
		10[a]	~200	0.75 (2) 0.35 (60)	

[a]Samples with thicknesses close to the arbitrary 10-nm mark for comparison.

impacts on both the magnetic arrangements and the system magnetic anisotropy due to the altered distances between neighboring Cr atoms and the canted nature of added spins. For the binary Cr_xTe_y system, the competition between antiferromagnetic Cr-Cr direct exchange interaction and ferromagnetic t^3-t^3 superexchange interaction in the Cr-Te-Cr unit is predominant in determining the overall magnetism.[22] In a relaxed Cr_xTe_y structure, neighboring Cr cations are separated enough that spins can only be mediated by a mutual Te anion to adhere to an energetically favored parallel arrangement. However, provided the distance between Cr pairs is shortened, sufficient overlapping of electronic clouds between neighboring Cr cations results in a non-negligible direct exchange interaction, which according to the Bethe-Slater curve, abides an antiparallel spin arrangement since it is more energetically favored.[24] Nonetheless, owing to the prevailing FM ordering manifested in the Cr_xTe_y family, it is rational to assume that the Cr-Te-Cr superexchange interaction is dominating overall. Therefore, the impact of Cr intercalants on the superexchange interaction would first be qualitatively analyzed.

Besides introducing more spins to the system, enhancing the superexchange interaction among Cr-Te-Cr units is a significant impact of additional Cr atoms in the intercalating layer. As compared to the initial Cr-Te-Cr angle, which is near 90°, in the $CrTe_2$ backbone, interlayer Cr atoms can form a Cr-Te-Cr unit with a much larger angle of about 132.0° (Figures 5A and 5B). Since the superexchange interaction is dominated by the largest M-X-M (M for magnetic cation and X for anion) angle, the new Cr-Te-Cr units intuitively show more significant FM coupling.[24] Notably, since the insertion of Cr atoms also distorts their surroundings, the magnetic contribution from the Cr-Te-Cr angles in the backbone would also be affected. As mentioned in the structural analysis, a Cr intercalant pulls planar Cr atoms closer in the interplanar direction. This pulling is also likely to result in a shortened distance between planar Cr atoms according to the strain analysis work.[24,25] Therefore, the Cr-Te-Cr angles inside 1T-$CrTe_2$ backbones become smaller, hence reducing the FM coupling. However, owing to the positive trend between Cr intercalants amount and T_C, it could be inferred that the impact of distortion is insignificant as compared to the contribution from numerous new Cr-Te-Cr units introduced. Notably, the spin direction of new Cr-Te-Cr units is not out-of-plane considering their oriented position relative to those in the $CrTe_2$ backbones. As such, Cr intercalants also result in noncollinearity to the spin conditions, which would be illustrated in detail.

A quantitative analysis of Cr intercalants' spin moments conveniently acknowledges the noncollinearity in the spin system of Cr_xTe_y. Taking CrTe as an example and assuming a perfect collinear spin configuration, the average magnetic moment of each Cr atom in an ultrathin CrTe crystal, obtained from the analyses of DOSs and spin density, is estimated to be about 4.29 μB (Figure 5C), showing a marked improvement

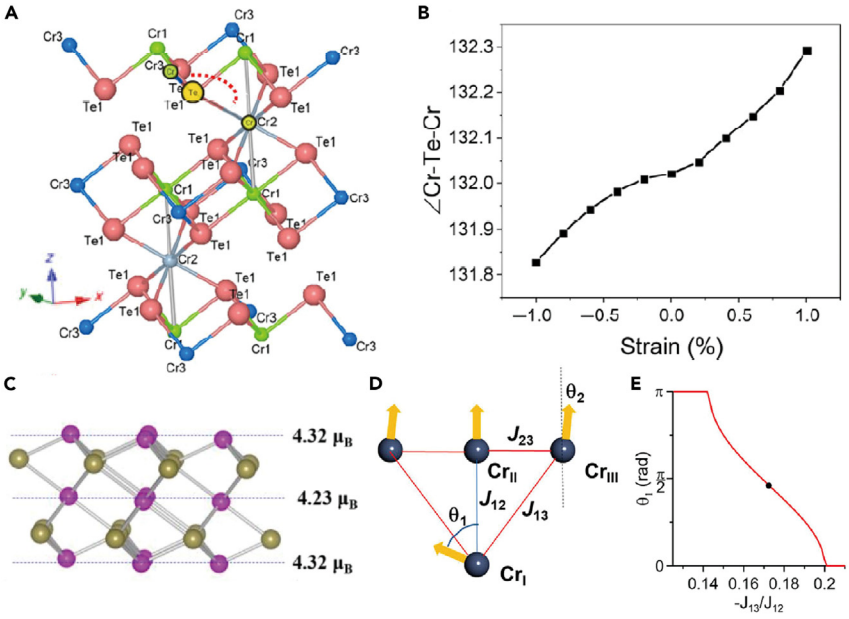

Figure 5. Models to elucidate the contribution of chromium intercalants to overall spins

(A–C) (A) The atomic structure of Cr_2Te_3 in the side view shows the position of the maximal Cr-Te-Cr angle. (B) The influence of biaxial strain on the maximal Cr-Te-Cr angle (reproduced with permission from Zhong et al.[24] Copyright 2021 Springer Nature Limited) C) The calculated atomic magnetic moments in few-UC CrTe (reproduced with permission from Wu et al.[17] Copyright 2021 Springer Nature Limited).

(D and E) (D) Illustration of spin canting in Cr_2Te_3: spin model demonstrates both the competition between spin exchange and spin canting. Canting angle θ_1 as a function of the ratio of second-nearest to nearest neighbor exchange parameters (reproduced with permission from Bian et al.[49] Copyright 2020 Informa UK Limited).

compared to 3.95 and 4.13 μB for bulk and thick CrTe crystals, respectively.[17] Intuitively, ultrathin CrTe expectedly possesses higher T_C and larger saturation magnetization compared to its bulk counterpart, which however contradicted the observation made by Wu et al.[17] This apparent discrepancy is explained by the structural disorder, which alters the local arrangement and thus the distance between Cr-Cr pairs. Therefore, the ideal FM coupling throughout the structure would be converted to a combination of both FM couplings with reduced exchange strength in elongated Cr-Cr pairs, and AFM couplings caused in much-shortened Cr-Cr pairs. Consequently, the spin polarization is drastically undermined with a significant decrease in the atomic magnetic moment to 0.84 μB. Also, considering the small magnetic moment difference of 0.09 μB between backbone and intercalating Cr, it could be inferred that not all spins in Cr intercalants are opposite to those of the backbone Cr since otherwise the average atomic magnetic moment would become negligible. Therefore, instead of a collinear spin system with partial interlayer AFM coupling, a noncollinear spin system seems more energetically favorable.

The spin canting model can effectively address the overestimation of magnetization in theory and illustrate the noncollinearity introduced by Cr intercalants. In a typical local atomic arrangement of Cr atoms found in Cr_2Te_3 crystal (Figure 5D), Cr atoms are classified into three types: Cr_I for those located in the vacancy layer whereas Cr_{II} and Cr_{III} in $CrTe_2$ backbones. The latter two could be further distinguished by the number of direct neighbors along the c-direction: Cr_{II} has no neighbor while Cr_{III} has one. Due to the different coordination conditions, magnetic moments for three types of Cr atoms are different from the density functional theory (DFT) calculation. Nonetheless, the average magnetization per Cr is calculated to be 3.03 μB assuming spins are arranged in a collinear manner, which is significantly larger than the experimental values. On that account, it seems logical that some spins are organized in canted directions to cancel out the spin moments partially. Cr_{II} assumes an ideal out-of-plane spin due to its symmetric surroundings. However, the spin directions of both Cr_I and Cr_{III} are deviated from the perfect out-of-plane directions, indicated by the blue and black dotted lines, respectively, forming polar angles θ_1 for Cr_I and θ_2 for Cr_{III} atoms. These angles originate from spin frustration and the unbalanced competing exchange interaction stemming from the nearest and second nearest neighbors.[49] Due to the presence of lateral

neighbors for Cr_{III}, θ_2 is sufficiently small to be neglected. On the other hand, polar angle θ_1 for Cr_I in the vacancy layer tends to change more vigorously under the competition between exchange interaction between nearest and second nearest neighbors. Such a competition could be quantified in terms of the ratio of interlayer exchange strength $-J_{12}/J_{13}$ under the scaffolds of the Heisenberg model. The Cr_I maintains a perfect AFM order (180° to the neutral line) to Cr_{II} at a relatively large range up until the $-J_{13}/J_{12}$ reaches about 0.145 (Figure 5E). A canted AFM order is maintained until $-J_{12}/J_{13}$ breaches the threshold value of about 0.17. Beyond this point, Cr_I starts to adopt a canted FM order relative to the closest Cr_{II}. Ideally, a perfect FM arrangement could be attained if the exchange integral ratio reaches 0.2 as seen from the plot. The black dot in the plot exemplifies the calculated angle of about 81° on the foundation of the experimental lattice constant, which cogently explains the substantial drop in the average spin moment to 2.37 μB per Cr in Cr_2Te_3. Theoretically, canted spin model persists throughout all Cr_xTe_y phases with an incompletely filled intercalation layer due to the similarities in the local atomic arrangement. Provided the increased Cr intercalant is sufficient to increase the interplanar Cr-Cr distance yet to change the coordination conditions of a single Cr_I atom, the $-J_{13}/J_{12}$ ratio intuitively becomes larger due to the smaller angle formed by the two integrals. The canted angle of Cr_I hence becomes smaller, leading to a greater contribution to the overall magnetization in FM order.

Recent studies have established a monotonically positive relationship between the T_C and Cr contents. Zhang et al. reported an increase of T_C from 200 K to 313 K in layered $Cr_{5+x}Te_8$ (x = −0.10, 0.11, 0.56, 1) while Fujisawa et al. found a similar trend from 160 K to 350 K in $Cr_{1+\delta}Te_2$ with δ ranging from 0.33 to 0.82.[97,98] Furthermore, both works reported the reorientation or isotropization of magnetic anisotropy with increasing Cr intercalants. These trends could be well addressed by a DFT calculation based on CrTe and $CrTe_2$ at the two stoichiometric extremes of Cr_xTe_y (Figure 6). $CrTe_2$ has only one Cr atom per unit cell and therefore only one type of exchange interaction—the intrasublattice exchange interaction J_{11} (green arrows in Figure 6A). In contrast, CrTe has two sublattices per unit cell so that both intrasublattice exchange interactions J_{11} and J_{22} (not shown for simplicity), and intersublattice exchange interaction J_{12} exist (red arrows in Figure 6B). Exchange interaction energies of J_{11}, J_{22}, and J_{12} with respect to the atomic distance are shown for both structures (Figures 6C and 6D). Due to the equivalent structure of two sublattices, J_{11} and J_{22} shall behave similarly, as represented by the completely overlapped plots. The intrasublattice interactions show a consistent FM coupling across all atomic distances in both structures. However, the intersublattice interaction J_{12} shows a mix of FM and AFM couplings with the Cr neighbors at various distances. The interplay of these interactions is essential to addressing the changes in magnetic properties. Owing to the strong intersublattice exchange interaction J_{12}, the effective exchange field strength at each Cr site shows an increasing trend with δ, therefore a monotonic increase in T_C.[98] Notably, the effective exchange field is determined by adding up all exchange interactions on one Cr site, and the calculation details are provided by the above-mentioned work. Furthermore, the breaking of collinearity in spins with increasing δ has been demonstrated by a series of schematics (Figure 6E). When $\delta = 0$, all spins are aligned FM out-of-plane. When δ increases, the intercalated Cr tends to align AF with respect to the original layers and meanwhile induces noncollinearity. The noncollinearity in self-intercalated Cr_xTe_y has been corroborated by several studies.[99,100] A typical method is to calculate the ratio α of the effective paramagnetic moment (m_c) to the experimental saturation moment (m_s) assuming the FM state is collinear. The presence of a noncollinear spin configuration would be evidenced by a deviation of α from 1. For a certain CrTe system, the α value is estimated to be ~1.6 provided the data are collected at 4.2 K, proving the noncollinear spin arrangement in the system.

INTRIGUING MAGNETIC BEHAVIOR OF Cr_xTe_y

A shift of easy-axis direction is predicted or observed in some Cr_xTe_y phases. 1T-$CrTe_2$ demonstrates a change of easy axis from in-plane to out-of-plane when the thickness is reduced. Figures 7A–7D show the magnetic property profiles of a 40-nm-thick and a 3-nm-thick sample when an external field is applied in an out-of-plane direction and in-plane direction, respectively. The much larger hysteresis loop in the in-plane external field B-H plot (Figure 7B) compared to the out-of-plane external field B-H plot (Figure 7A) suggests the easy axis is leaning toward the in-plane direction. On the contrary, the in-plane hysteresis loop completely vanishes when thickness drops to 3 nm (Figure 7D), whereas the out-of-plane hysteresis preserves (Figure 7C). As such, the ultrathin 1T-$CrTe_2$ has an ideal out-of-plane easy axis of spins. Referring to the upper panel (Figure 7E) which describes the relations between coercive field and thickness for both directions, it could be easily extracted that the out-of-plane magnetization remains unchanged while the in-plane magnetization diminishes with reducing thicknesses. The critical thickness for the shift in the

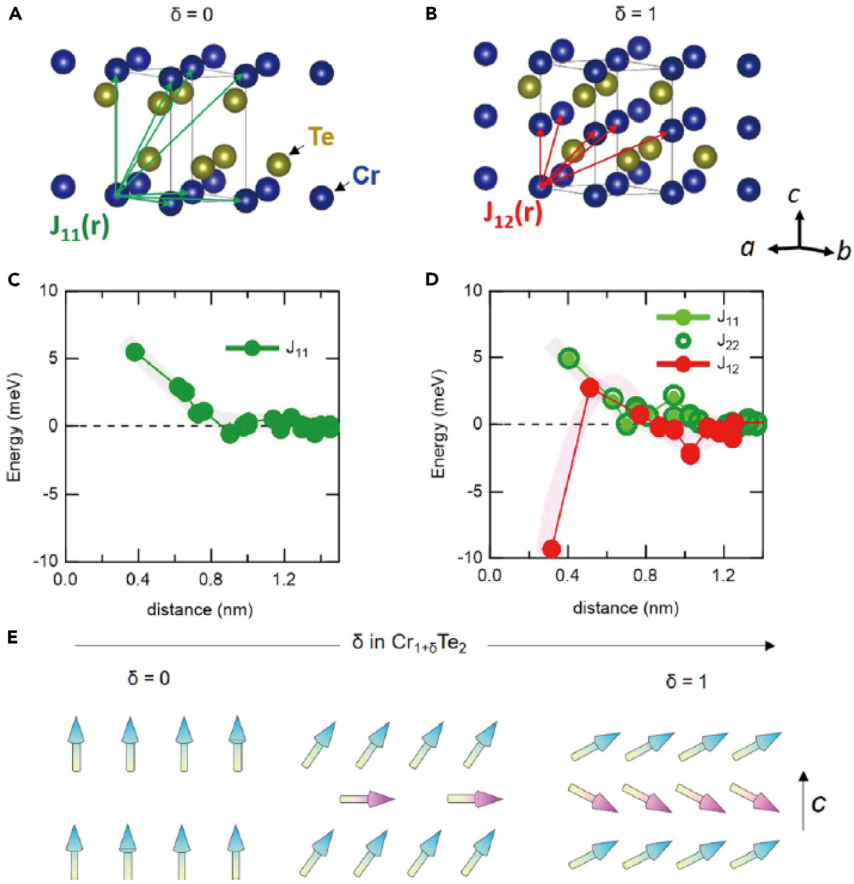

Figure 6. Evolution of exchange interaction for $Cr_{1+\delta}Te_2$ (A–E) crystal structures

(A–D) $CrTe_2$ (δ = 0) and (B) CrTe (δ = 1). Green and red arrows indicate direct exchange interactions for pairs of atoms intrasublattice (J_{11}) and intersublattice (J_{12}), respectively. For simplicity, interlayer contributions J_{11} and J_{22} are not shown in (B). DFT-calculated exchange interactions J_{11}, J_{22}, and J_{12} as a function of atomic separation for (C) $CrTe_2$ and (D) CrTe. Thick shades demonstrate the trend of exchange interactions with atomic distance.

(E) Schematic of the expected evolution of ground-state magnetic configuration of $Cr_{1+\delta}Te_2$, with individual arrows indicating the local spins. (reproduced with permission from Fujosawa et al.[98] Copyright 2020 American Physical Society).

easy axis is also estimated to be about 10 nm as seen from the plot. Meng et al. suggest the weakening of the Coulomb screening in the 2D limit is predominant to the shift in easy axis.[47] Provided monolayer $CrTe_2$ has sufficient on-site Coulomb potential, the magnetic anisotropy energy (MAE) sign can change from negative to positive, indicating the flipping of the easy axis from in-plane direction to out-of-plane direction (Figure 7F). However, for bulk $CrTe_2$, the negative MAE, which implies in-plane preference, persists along any range of Coulomb potential. More importantly, since the effective Coulomb screening is significantly weakened in ultrathin 2D material due to the quantum confinement, high on-site Coulomb potential for monolayer $CrTe_2$ is easily attained when the material interacts with the substrate. The thickness dependency of magnetic properties explored in 1T-$CrTe_2$ and surface engineering potential inspire ways of improving or tuning the magnetic properties in Cr_xTe_y material.

Notably, Cr_5Te_8 with the same composition can exist in different phases through careful control of synthesis conditions. The trigonal and monoclinic Cr_5Te_8, with ultrathin thickness and environmental stability, have been prepared.[28] tr-Cr_5Te_8 and m-Cr_5Te_8 can be differentiated by the arrangement of intercalating Cr intercalants. Intercalating layers are arranged in the relatively same set of positions in tr-Cr_5Te_8 as indicated by Cr_{II} whereas intercalating layers are located at two sets of positions alternatingly in m-Cr_5Te_8 as indicated by Cr_{II} and Cr'_{II} (Figure 7G). Structural difference intuitively causes variation in magnetic properties. Hysteresis plots of both phases have been put aside (Figures 7H and 7I) and an obvious elevation of T_C of about 25 K has been spotted in m-Cr_5Te_8 as compared to the trigonal counterpart of the same thickness of

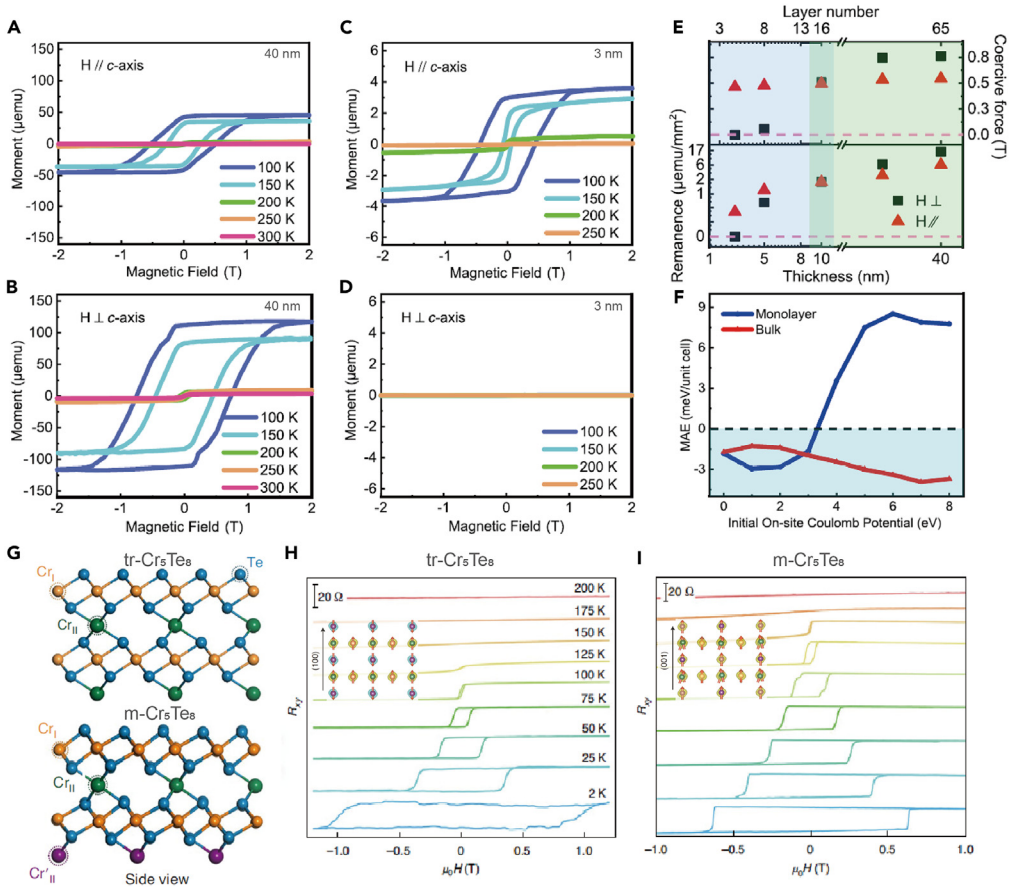

Figure 7. Intriguing magnetic behavior of Cr_xTe_y

(A–F) The thickness-dependent magnetic anisotropy of 1T-$CrTe_2$: The magnetic hysteresis plots for a sample with a thickness of 40 nm under (A) parallel and (B) vertical fields to the c axis. The magnetic hysteresis plots for a sample with a thickness of 3 nm under (C) parallel and (D) vertical fields to the c axis. (E) Remanence and coercivity trends of various thicknesses. (F) The DFT-calculated magnetic anisotropy energy (MAE) as a function of initial on-site Coulomb potential for monolayer and bulk 1T-$CrTe_2$ (reproduced with permission from Meng et al.[47] Copyright 2021 Springer Nature Limited).

(G–I) (G) Structural difference in monoclinic and trigonal Cr_5Te_8 demonstrated in the side views. (H) The magnetic hysteresis plots of 6-nm tr-Cr_5Te_8 with an inset illustrate the calculated spin configuration. (I) The magnetic hysteresis plots of 6-nm m-Cr_5Te_8 Cr_5Te_8 with inset illustrating the calculated spin configuration (reproduced with permission from Tang et al.[28] Copyright 2022 Springer Nature Limited).

6 nm. Also, 6-nm-thick m-Cr_5Te_8 has also been reported to have a stronger coercivity of about 1.4 T as compared to that of tr-Cr_5Te_8 of about 0.8 T under 2.5 K temperature. The augmented overall spin can be elucidated by the simulated spin orderings in both phases shown in the insets. The spin polarizations of all three groups of Cr atoms, Cr_I, Cr_{II}, and Cr'_{II}, in m-Cr_5Te_8 are parallel with slight spin canting of Cr_I occurring, whereas the spins of Cr_{II} layers are antiparallel in tr-Cr_5Te_8. Notably, the relevant spin arrangements result in a much larger average net magnetic moment of m-Cr_5Te_8, 3.76 μB compared to the 2.06 μB of tr-Cr_5Te_8. This work enriches the impact of Cr intercalants on the overall spin of the Cr_xTe_y material system in that rather than the amount of Cr intercalants; the exact positions of added Cr atoms are more vital to the performance. Moreover, it also inspires the exploration and engineering of potentially novel phases in Cr_xTe_y.

CONCLUSION AND OUTLOOK

The conserving of magnetic ordering in the 2D limit has been corroborated by the realization of atomically thin CrI_3 and $CrGeTe_3$. Ever since, the interest in exploring 2D magnets of higher transition temperatures, better magnetic properties, and greater stability has been sparked for academic and application purposes.

In the past few years, 2D Cr_xTe_y has become a heated material class for its ideal intrinsic magnetism and rich stoichiometries. The detailed structural differences are elaborated using simulated atomic structures. Using the CVD approach alone, ultrathin Cr_xTe_y of various phases has been prepared to display various magnetic properties. Furthermore, conventionally used probing techniques for 2D magnets have been introduced and compared, and the magnetic properties of current Cr_xTe_y candidates are summarized. Moreover, how Cr intercalants contribute to the overall magnetic properties is carefully elucidated by the explanation of the Cr-Te-Cr superexchange interaction and spin canted model. In addition, the monotonic increase in T_C and isotropization with increasing Cr content is also cautiously clarified by theoretical calculation. Notably, several intriguing phenomena have been discovered in Cr_xTe_y, including thickness dependency of easy-axis direction, surface-tunable magnetic properties, and phase dependency of the overall spin moment, showcasing Cr_xTe_y's capability as a platform for fundamental studies as well as practical applications.

To better evaluate the impact of Cr intercalants on magnetic properties and explain the contrary of theoretical predictions and actual performance summarized from previous studies, accurate magnetic characterization of a comprehensive collection of Cr_xTe_y using the same standards is the prerequisite. The trend mentioned above could be erroneous or incomplete since data are collected from various reports using samples of different thicknesses, which are tested with different techniques. Magnetic properties of Cr_xTe_y are highly thickness dependent and sensitive to the testing environment. Benchmarking the magnetic properties of different phases, in criteria of sample dimensions, consistency in characterization methods, and strict control on testing conditions, e.g., temperature and external field strengths, is necessary. As such, the correlation between the phase/composition and magnetic properties of Cr_xTe_y, e.g., T_C, coercive field strengths, and even remanence and magnetic anisotropy, could be reliably extracted and studied.

Due to the complexity of Cr_xTe_y in terms of phases and compositions, there is plenty of room for further improvement of material synthesis. Phase controllability is one of the vital targets as it enables convenient and effective control of material phases and associated properties, which is conducive to both academic and practical goals. As discussed in the synthesis part, several parameters such as temperatures, carrier gas, and precursors have significant effects on the final compositions and phases of the synthesized materials. However, no unifying trend has been summarized to aid the phase-selective synthesis. Therefore, an in-depth investigation of the effect of various growth parameters is required both experimentally and theoretically. A collection of synthesis conditions to ascertain a known phase is also pragmatic and beneficial to controlled synthesis. Furthermore, effective simulation methods aided by machine learning are believed to be a promising tool to precisely describe some of the previously abstract variables, enabling advanced control and selection of synthesis parameters.[101,102]

For practical uses, a challenge common to most 2D materials is also encountered: reaching a large size while maintaining ultrathin thickness. To our best knowledge, the largest 2D Cr_xTe_y nanoflakes reported so far are CrTe with a size of about 250 μm and a thickness of 5 nm, and Cr_2Te_3 with a size of 190 μm and a thickness of 5.1 nm, prepared by APCVD.[51,62] Notably, Wen et al. used a similar technique to prepare a large-sized Cr_2Te_3 of 0.73 mm with a thickness of 19.5 nm and a millimeter-scale sample of 0.93 mm without thickness specified.[51] The reported sizes for 2D nanoflakes of other compositions range up to about 50 μm.[19,27,47] Hence, methods for wafer-size and minimal defects synthesis are urgently required for their future application in spintronic and magnetic devices. A few strategies could be adopted from reported synthesis methods for other 2D TMDCs. Direct tellurization of a thin Cr layer deposited on the target substrate could ensure an epitaxial growth of a few TMDCs with decent coverage, as evidenced by the $PdTe_2$ and $PtTe_2$.[103] However, an ultrahigh vacuum is required to ascertain the good quality of the final products, and thus, customization to the CVD setup is needed. Moreover, organic seeding promoters, used in the case of monolayer MoS_2, provide another approach as they can provide initial nuclei to facilitate the epitaxial growth and thus lower the growth temperature.[104] Also, owing to the low sublimation/decomposition temperature of seeding promoters, for example, PTAS, CuPc, PTCDA, etc., no contamination of the final products would happen. In addition, metal-organic CVD and special design of the precursors are other possible solutions since the wafer-size synthesis of several 2D TMDCs has been realized using these techniques.[105–107]

Pure phase synthesis is another essential goal for 2D materials, especially for the Cr_xTe_y family with complex compositions and phases. A convenient approach is to accurately control the growth temperature due to the small differences in ground-state energies among these compositions and phases. Li et al. have

reported the controlled synthesis of 2H-$MoTe_2$ and 1T′-$MoTe_2$ by setting the growth temperature at 670°C and 710°C, respectively, due to the higher energy of 1T′-$MoTe_2$ by ~0.03 eV.[108] Similarly, the above-mentioned distorted m-Cr_5Te_8 could be selectively prepared by freezing this less stable phase via increasing the cooling rate.[28] Furthermore, tuning the stability of the salt-induced metastable intermediates in salt-assisted CVD is another potential technique. Increasing the potassium concentration in the K_xMoS_2 beyond the critical point of 44% is proven useful in facilitating the formation of the 1T′-K_xMoS_2 and thus 1T′-MoS_2.[109] The uniformity of the product could also be improved by subsiding the vapor concentration gradient of reactants flowing through the target substrate. This is commonly achieved by introducing a confined environment for the reaction using an inner tube to accommodate reactants and substrate.[19,110] To realize even higher uniformity, the post-growth annealing process at designed temperatures is proven effective. CrTe is preferably transformed from other Cr_xTe_y under the prolonged high-temperature annealing as high temperature will induce the loss of Te and subsequent reconstruction.[57,98]

In the frontline fundamental research perspective, direct synthesis of heterostructures based on different phases of Cr_xTe_y becomes a growingly popular direction. For the ferromagnetic family of Cr_xTe_y, the heterostructures provide a model system to realize the control of magnetic anisotropy or overall magnetic behavior.[111] For example, Niu et al. have prepared lateral Cr_2Te_3-Cr_5Te_8 heterojunction in a one-pot CVD method.[112] The lateral heterojunction displays controllability in magnetic moments by an external field, suggested by the sharp steps in the hysteresis loop. The decoupling effect, arising from the random arrangement of Cr intercalants, is predicted to be the reason behind the flipping behavior. Furthermore, a fascinating magnetic phenomenon, Néel-type skyrmion, has been observed in single-phase $Cr_{1.3}Te_2$ using Lorentz transmission electron microscopy.[26] This compound exhibits a novel 3D ordered (2 × 2 × 2) supercell with an asymmetric filling of the two inequivalent vdW gaps, which breaks the inversion symmetry of the structure and thus lays the foundation for chiral magnetic nanostructures. Owing to the rich possibilities in phases and combinations, it is believed that Cr_xTe_y is a reliable platform to explore and manipulate novel magnetic properties in the 2D realm. More attention and resources are encouraged to be pooled into this material system to further unlock its practical and academic potential.

ACKNOWLEDGMENTS

Z.L. acknowledges the support from National Research Foundation, Singapore, under its Competitive Research Program (CRP) (NRF-CRP22-2019-0007 and NRF-CRP22-2019-0004), under its NRF-ISF joint research program (NRF2020-NRF-ISF004-3520). This research is also supported by A*STAR under its AME IRG Grant (Project No. A2083c0052).

AUTHOR CONTRIBUTIONS

All authors wrote and edited this review article.

DECLARATION OF INTERESTS

The authors declare no competing interests.

REFERENCES

1. Wang, Z., Zhang, T., Ding, M., Dong, B., Li, Y., Chen, M., Li, X., Huang, J., Wang, H., Zhao, X., et al. (2018). Electric-field control of magnetism in a few-layered van der Waals ferromagnetic semiconductor. Nat. Nanotechnol. *13*, 554–559. https://doi.org/10.1038/s41565-018-0186-z.

2. Gong, S.-J., Gong, C., Sun, Y.-Y., Tong, W.-Y., Duan, C.-G., Chu, J.-H., and Zhang, X. (2018). Electrically induced 2D half-metallic antiferromagnets and spin field effect transistors. Proc. Natl. Acad. Sci. USA *115*, 8511–8516. https://doi.org/10.1073/pnas.1715465115.

3. Jiang, S., Li, L., Wang, Z., Shan, J., and Mak, K.F. (2019). Spin tunnel field-effect transistors based on two-dimensional van der Waals heterostructures. Nat. Electron. *2*, 159–163. https://doi.org/10.1038/s41928-019-0232-3.

4. Liu, Z., Deng, L., and Peng, B. (2021). Ferromagnetic and ferroelectric two-dimensional materials for memory application. Nano Res. *14*, 1802–1813. https://doi.org/10.1007/s12274-020-2860-3.

5. Tong, L., Peng, Z., Lin, R., Li, Z., Wang, Y., Huang, X., Xue, K.-H., Xu, H., Liu, F., Xia, H., et al. (2021). 2D materials–based homogeneous transistor-memory architecture for neuromorphic hardware. Science *373*, 1353–1358. https://doi.org/10.1126/science.abg3161.

6. Dieny, B., Sousa, R.C., Hérault, J., Papusoi, C., Prenat, G., Ebels, U., Houssameddine, D., Rodmacq, B., Auffret, S., Prejbeanu-Buda, L., et al. (2011). Chapter two - spintronic devices for memory and logic applications. In Handbook of Magnetic Materials, K.H.J. Buschow, ed. (Elsevier), pp. 107–127. https://doi.org/10.1016/B978-0-444-53780-5.00002-8.

7. Ahn, E.C. (2020). 2D materials for spintronic devices. npj 2D Mater. Appl. *4*, 17. https://doi.org/10.1038/s41699-020-0152-0.

8. Liu, Y., Zeng, C., Zhong, J., Ding, J., Wang, Z.M., and Liu, Z. (2020). Spintronics in two-dimensional materials. Nano-Micro Lett. *12*, 93. https://doi.org/10.1007/s40820-020-00424-2.

9. Ikeda, S., Hayakawa, J., Ashizawa, Y., Lee, Y.M., Miura, K., Hasegawa, H., Tsunoda, M., Matsukura, F., and Ohno, H. (2008). Tunnel magnetoresistance of 604% at 300K by suppression of Ta diffusion in CoFeB/MgO/CoFeB pseudo-spin-valves annealed at high temperature. Appl. Phys. Lett. *93*, 082508. https://doi.org/10.1063/1.2976435.

10. Gong, C., Li, L., Li, Z., Ji, H., Stern, A., Xia, Y., Cao, T., Bao, W., Wang, C., Wang, Y., et al. (2017). Discovery of intrinsic ferromagnetism in two-dimensional van der Waals crystals. Nature *546*, 265–269. https://doi.org/10.1038/nature22060.

11. Huang, B., Clark, G., Navarro-Moratalla, E., Klein, D.R., Cheng, R., Seyler, K.L., Zhong, D., Schmidgall, E., McGuire, M.A., Cobden, D.H., et al. (2017). Layer-dependent ferromagnetism in a van der Waals crystal down to the monolayer limit. Nature *546*, 270–273. https://doi.org/10.1038/nature22391.

12. Fei, Z., Huang, B., Malinowski, P., Wang, W., Song, T., Sanchez, J., Yao, W., Xiao, D., Zhu, X., May, A.F., et al. (2018). Two-dimensional itinerant ferromagnetism in atomically thin Fe3GeTe2. Nat. Mater. *17*, 778–782. https://doi.org/10.1038/s41563-018-0149-7.

13. Deng, Y., Yu, Y., Song, Y., Zhang, J., Wang, N.Z., Sun, Z., Yi, Y., Wu, Y.Z., Wu, S., Zhu, J., et al. (2018). Gate-tunable room-temperature ferromagnetism in two-dimensional Fe3GeTe2. Nature *563*, 94–99. https://doi.org/10.1038/s41586-018-0626-9.

14. Liu, H., Bao, L., Zhou, Z., Che, B., Zhang, R., Bian, C., Ma, R., Wu, L., Yang, H., Li, J., et al. (2019). Quasi-2D transport and weak antilocalization effect in few-layered VSe2. Nano Lett. *19*, 4551–4559. https://doi.org/10.1021/acs.nanolett.9b01412.

15. Gao, D., Xue, Q., Mao, X., Wang, W., Xu, Q., and Xue, D. (2013). Ferromagnetism in ultrathin VS2 nanosheets. J. Mater. Chem. C *1*, 5909–5916. https://doi.org/10.1039/C3TC31233J.

16. Zhang, X., Lu, Q., Liu, W., Niu, W., Sun, J., Cook, J., Vaninger, M., Miceli, P.F., Singh, D.J., Lian, S.-W., et al. (2021). Room-temperature intrinsic ferromagnetism in epitaxial CrTe2 ultrathin films. Nat. Commun. *12*, 2492. https://doi.org/10.1038/s41467-021-22777-x.

17. Wu, H., Zhang, W., Yang, L., Wang, J., Li, J., Li, L., Gao, Y., Zhang, L., Du, J., Shu, H., and Chang, H. (2021). Strong intrinsic room-temperature ferromagnetism in freestanding non-van der Waals ultrathin 2D crystals. Nat. Commun. *12*, 5688. https://doi.org/10.1038/s41467-021-26009-0.

18. Sun, X., Li, W., Wang, X., Sui, Q., Zhang, T., Wang, Z., Liu, L., Li, D., Feng, S., Zhong, S., et al. (2020). Room temperature ferromagnetism in ultra-thin van der Waals crystals of 1T-CrTe2. Nano Res. *13*, 3358–3363. https://doi.org/10.1007/s12274-020-3021-4.

19. Chen, C., Chen, X., Wu, C., Wang, X., Ping, Y., Wei, X., Zhou, X., Lu, J., Zhu, L., Zhou, J., et al. (2022). Air-stable 2D Cr5Te8 nanosheets with thickness-tunable ferromagnetism. Adv. Mater. *34*, 2107512. https://doi.org/10.1002/adma.202107512.

20. Tang, B., Hu, D., Zhao, X., Wang, X., and Liu, Z. (2022). Recent developments in chemical vapor deposition of 2D magnetic transition metal chalcogenides. ACS Appl. Electron. Mater. *4*, 3303–3324. https://doi.org/10.1021/acsaelm.2c00425.

21. Gao, P., Li, X., and Yang, J. (2021). Thickness dependent magnetic transition in few layer 1T phase CrTe2. J. Phys. Chem. Lett. *12*, 6847–6851. https://doi.org/10.1021/acs.jpclett.1c01901.

22. Lv, H.Y., Lu, W.J., Shao, D.F., Liu, Y., and Sun, Y.P. (2015). Strain-controlled switch between ferromagnetism and antiferromagnetism in 1T-CrX_2 (X=Se, Te) monolayers. Phys. Rev. B *92*, 214419. https://doi.org/10.1103/PhysRevB.92.214419.

23. Wang, Y., Wang, C., Liang, S.-J., Ma, Z., Xu, K., Liu, X., Zhang, L., Admasu, A.S., Cheong, S.-W., Wang, L., et al. (2020). Strain-sensitive magnetization reversal of a van der Waals magnet. Adv. Mater. *32*, 2004533. https://doi.org/10.1002/adma.202004533.

24. Zhong, J., Wang, M., Liu, T., Zhao, Y., Xu, X., Zhou, S., Han, J., Gan, L., and Zhai, T. (2022). Strain-sensitive ferromagnetic two-dimensional Cr2Te3. Nano Res. *15*, 1254–1259. https://doi.org/10.1007/s12274-021-3633-3.

25. Zhou, J., Song, X., Chai, J., Wong, N.L.M., Xu, X., Jiang, Y., Feng, Y.P., Yang, M., and Wang, S. (2022). Structure dependent and strain tunable magnetic ordering in ultrathin chromium telluride. J. Alloys Compd. *893*, 162223. https://doi.org/10.1016/j.jallcom.2021.162223.

26. Saha, R., Meyerheim, H.L., Göbel, B., Hazra, B.K., Deniz, H., Mohseni, K., Antonov, V., Ernst, A., Knyazev, D., Bedoya-Pinto, A., et al. (2022). Observation of Néel-type skyrmions in acentric self-intercalated Cr1+δTe2. Nat. Commun. *13*, 3965. https://doi.org/10.1038/s41467-022-31319-y.

27. Li, B., Deng, X., Shu, W., Cheng, X., Qian, Q., Wan, Z., Zhao, B., Shen, X., Wu, R., Shi, S., et al. (2022). Air-stable ultrathin Cr3Te4 nanosheets with thickness-dependent magnetic biskyrmions. Mater. Today *57*, 66–74. https://doi.org/10.1016/j.mattod.2022.04.011.

28. Tang, B., Wang, X., Han, M., Xu, X., Zhang, Z., Zhu, C., Cao, X., Yang, Y., Fu, Q., Yang, J., et al. (2022). Phase engineering of Cr5Te8 with colossal anomalous Hall effect. Nat. Electron. *5*, 224–232. https://doi.org/10.1038/s41928-022-00754-6.

29. Onsager, L. (1944). Crystal statistics. I. A two-dimensional model with an order-disorder transition. Phys. Rev. *65*, 117–149. https://doi.org/10.1103/PhysRev.65.117.

30. Elmers, H.-J. (1995). Ferromagnetic monolayers. Int. J. Mod. Phys. B *09*, 3115–3180. https://doi.org/10.1142/S0217979295001191.

31. Hellman, F., Hoffmann, A., Tserkovnyak, Y., Beach, G.S.D., Fullerton, E.E., Leighton, C., MacDonald, A.H., Ralph, D.C., Arena, D.A., Dürr, H.A., et al. (2017). Interface-induced phenomena in magnetism. Rev. Mod. Phys. *89*, 025006. https://doi.org/10.1103/RevModPhys.89.025006.

32. Cremer, J.T. (2013). 8 - coherent, inelastic, magnetic neutron scatter, spin waves, and magnons. In Neutron and X-ray Optics, J.T. Cremer, ed. (Elsevier), pp. 393–454. https://doi.org/10.1016/B978-0-12-407164-3.00007-3.

33. Hilscher, G., and Michor, H. (2005). Magnetic interactions. In Encyclopedia of Condensed Matter Physics, F. Bassani, G.L. Liedl, and P. Wyder, eds. (Elsevier), pp. 197–204. https://doi.org/10.1016/B0-12-369401-9/00515-5.

34. Gong, C., and Zhang, X. (2019). Two-dimensional magnetic crystals and emergent heterostructure devices. Science *363*, eaav4450. https://doi.org/10.1126/science.aav4450.

35. Hu, X., Zhao, Y., Shen, X., Krasheninnikov, A.V., Chen, Z., and Sun, L. (2020). Enhanced ferromagnetism and tunable magnetism in Fe3GeTe2 monolayer by strain engineering. ACS Appl. Mater. Interfaces *12*, 26367–26373. https://doi.org/10.1021/acsami.0c05530.

36. Alex Hubert, R.S. (1998). Magnetic Domains: The Analysis of Magnetic Microstructures, 1 Edition (Springer Berlin).

37. Meiklejohn, W.H., and Bean, C.P. (1957). New magnetic anisotropy. Phys. Rev. *105*, 904–913. https://doi.org/10.1103/PhysRev.105.904.

38. Gruszecki, P., Banerjee, C., Mruczkiewicz, M., Hellwig, O., Barman, A., and Krawczyk, M. (2021). Chapter Two - the influence of the internal domain wall structure on spin wave band structure in periodic magnetic stripe domain patterns. In Solid State Physics, R.E. Camley and R.L. Stamps, eds. (Academic Press), pp. 29–82. https://doi.org/10.1016/bs.ssp.2021.08.001.

39. Bozorth, R.M. (1978). Ferromagnetism (IEEE Press).

40. Holstein, T., and Primakoff, H. (1940). Field dependence of the intrinsic domain magnetization of a ferromagnet. Phys. Rev. *58*, 1098–1113. https://doi.org/10.1103/PhysRev.58.1098.

41. Lado, J.L., and Fernández-Rossier, J. (2017). On the origin of magnetic anisotropy in two dimensional CrI3. 2D Mater. *4*, 035002. https://doi.org/10.1088/2053-1583/aa75ed.

42. Goodenough, J.B. (1958). An interpretation of the magnetic properties of the perovskite-type mixed crystals La1−xSrxCoO3−λ. J. Phys. Chem. Solid. *6*, 287–297. https://doi.org/10.1016/0022-3697(58)90107-0.

43. Kanamori, J. (1959). Superexchange interaction and symmetry properties of electron orbitals. J. Phys. Chem. Solid. *10*,

87–98. https://doi.org/10.1016/0022-3697(59)90061-7.

44. Roemer, R., Liu, C., and Zou, K. (2020). Robust ferromagnetism in wafer-scale monolayer and multilayer Fe3GeTe2. npj 2D Mater. Appl. *4*, 33. https://doi.org/10.1038/s41699-020-00167-z.

45. Lotgering, F.K., and Gorter, E.W. (1957). Solid solutions between ferromagnetic and antiferromagnetic compounds with NiAs structure. J. Phys. Chem. Solid. *3*, 238–249. https://doi.org/10.1016/0022-3697(57)90028-8.

46. Zhao, X., Ning, S., Fu, W., Pennycook, S.J., and Loh, K.P. (2018). Differentiating polymorphs in molybdenum disulfide via electron microscopy. Adv. Mater. *30*, 1802397. https://doi.org/10.1002/adma.201802397.

47. Meng, L., Zhou, Z., Xu, M., Yang, S., Si, K., Liu, L., Wang, X., Jiang, H., Li, B., Qin, P., et al. (2021). Anomalous thickness dependence of Curie temperature in air-stable two-dimensional ferromagnetic 1T-CrTe2 grown by chemical vapor deposition. Nat. Commun. *12*, 809. https://doi.org/10.1038/s41467-021-21072-z.

48. Wang, M., Kang, L., Su, J., Zhang, L., Dai, H., Cheng, H., Han, X., Zhai, T., Liu, Z., and Han, J. (2020). Two-dimensional ferromagnetism in CrTe flakes down to atomically thin layers. Nanoscale *12*, 16427–16432. https://doi.org/10.1039/D0NR04108D.

49. Bian, M., Kamenskii, A.N., Han, M., Li, W., Wei, S., Tian, X., Eason, D.B., Sun, F., He, K., Hui, H., et al. (2021). Covalent 2D Cr2Te3 ferromagnet. Mater. Res. Lett. *9*, 205–212. https://doi.org/10.1080/21663831.2020.1865469.

50. Bian, M., Zhu, L., Wang, X., Choi, J., Chopdekar, R.V., Wei, S., Wu, L., Huai, C., Marga, A., Yang, Q., et al. (2022). Dative epitaxy of commensurate monocrystalline covalent van der Waals moiré supercrystal. Adv. Mater. *34*, 2200117. https://doi.org/10.1002/adma.202200117.

51. Wen, Y., Liu, Z., Zhang, Y., Xia, C., Zhai, B., Zhang, X., Zhai, G., Shen, C., He, P., Cheng, R., et al. (2020). Tunable room-temperature ferromagnetism in two-dimensional Cr2Te3. Nano Lett. *20*, 3130–3139. https://doi.org/10.1021/acs.nanolett.9b05128.

52. Wang, J., Wang, W., Fan, J., Zheng, H., Liu, H., Ma, C., Zhang, L., Tong, W., Ling, L., Zhu, Y., and Yang, H. (2022). Epitaxial growth and room-temperature ferromagnetism of quasi-2D layered Cr4Te5 thin film. J. Phys. D Appl. Phys. *55*, 165001. https://doi.org/10.1088/1361-6463/ac47c2.

53. Wang, W., Marefat, F., Mohseni, P., Kilgore, K., Najafizadeh, L., Zhang, L., Sun, Y., Wang, C., Zhu, Y., and Yang, H. (2022). Fabrication and magnetic–electronic properties of van der Waals Cr4Te5 ferromagnetic films. CrystEngComm *2022*, 674–677. https://doi.org/10.1039/D1CE01200B.

54. Liu, H., Fan, J., Zheng, H., Wang, J., Ma, C., Wang, H., Zhang, L., Wang, C., Zhu, Y., and Yang, H. (2022). Magnetic properties and critical behavior of quasi-2D layered Cr4Te5 thin film. Front. Physiol. *18*, 13302. https://doi.org/10.1007/s11467-022-1210-1.

55. Sagan, P., and Kuzma, M. (2012). THEED study of CrTe thin films obtained by pulsed laser deposition. Solid State Phenom. *186*, 172–176. https://doi.org/10.4028/www.scientific.net/SSP.186.172.

56. Chua, R., Zhou, J., Yu, X., Yu, W., Gou, J., Zhu, R., Zhang, L., Liu, M., Breese, M.B.H., Chen, W., et al. (2021). Room temperature ferromagnetism of monolayer chromium telluride with perpendicular magnetic anisotropy. Adv. Mater. *33*, 2103360. https://doi.org/10.1002/adma.202103360.

57. Lasek, K., Coelho, P.M., Gargiani, P., Valvidares, M., Mohseni, K., Meyerheim, H.L., Kostanovskiy, I., Zberecki, K., and Batzill, M. (2022). Van der Waals epitaxy growth of 2D ferromagnetic Cr(1+δ)Te2 nanolayers with concentration-tunable magnetic anisotropy. Appl. Phys. Rev. *9*, 011409. https://doi.org/10.1063/5.0070079.

58. Gong, Y., Ye, G., Lei, S., Shi, G., He, Y., Lin, J., Zhang, X., Vajtai, R., Pantelides, S.T., Zhou, W., et al. (2016). Synthesis of millimeter-scale transition metal dichalcogenides single crystals. Adv. Funct. Mater. *26*, 2009–2015. https://doi.org/10.1002/adfm.201504633.

59. Zhou, J., Liu, F., Lin, J., Huang, X., Xia, J., Zhang, B., Zeng, Q., Wang, H., Zhu, C., Niu, L., et al. (2017). Large-Area and high-quality 2D transition metal telluride. Adv. Mater. *29*, 1603471. https://doi.org/10.1002/adma.201603471.

60. Zhou, J., Lin, J., Huang, X., Zhou, Y., Chen, Y., Xia, J., Wang, H., Xie, Y., Yu, H., Lei, J., et al. (2018). A library of atomically thin metal chalcogenides. Nature *556*, 355–359. https://doi.org/10.1038/s41586-018-0008-3.

61. Coughlin, A.L., Xie, D., Yao, Y., Zhan, X., Chen, Q., Hewa-Walpitage, H., Zhang, X., Guo, H., Zhou, H., Lou, J., et al. (2020). Near degeneracy of magnetic phases in two-dimensional chromium telluride with enhanced perpendicular magnetic anisotropy. ACS Nano *14*, 15256–15266. https://doi.org/10.1021/acsnano.0c05534.

62. Guo, Y., Kang, L., Yu, S., Yang, J., Qi, X., Zhang, Z., and Liu, Z. (2021). CVD growth of large-scale and highly crystalline 2D chromium telluride nanoflakes. ChemNanoMat *7*, 323–327. https://doi.org/10.1002/cnma.202000650.

63. Suleman, M., Lee, S., Kim, M., Nguyen, V.H., Riaz, M., Nasir, N., Kumar, S., Park, H.M., Jung, J., and Seo, Y. (2022). NaCl-assisted temperature-dependent controllable growth of large-area MoS2 crystals using confined-space CVD. ACS Omega *7*, 30074–30086. https://doi.org/10.1021/acsomega.2c03108.

64. Astinchap, B., and Laelabadi, K.G. (2019). Effects of substrate temperature and precursor amount on optical properties and microstructure of CVD deposited amorphous TiO2 thin films. J. Phys. Chem. Solid. *129*, 217–226. https://doi.org/10.1016/j.jpcs.2019.01.012.

65. Lee, K., Kim, Y.S., and Joo, S.K. (1992). Effect of substrate temperature on the selectivity in low pressure chemical vapor deposition of aluminum. J. Electrochem. Soc. *139*, 3578–3581. https://doi.org/10.1149/1.2069125.

66. Cai, Z., Liu, B., Zou, X., and Cheng, H.-M. (2018). Chemical vapor deposition growth and applications of two-dimensional materials and their heterostructures. Chem. Rev. *118*, 6091–6133. https://doi.org/10.1021/acs.chemrev.7b00536.

67. Liu, B., Fathi, M., Chen, L., Abbas, A., Ma, Y., and Zhou, C. (2015). Chemical vapor deposition growth of monolayer WSe2 with tunable device characteristics and growth mechanism study. ACS Nano *9*, 6119–6127. https://doi.org/10.1021/acsnano.5b01301.

68. He, Y., Sobhani, A., Lei, S., Zhang, Z., Gong, Y., Jin, Z., Zhou, W., Yang, Y., Zhang, Y., Wang, X., et al. (2016). Layer engineering of 2D semiconductor junctions. Adv. Mater. *28*, 5126–5132. https://doi.org/10.1002/adma.201600278.

69. Chu, J., Zhang, Y., Wen, Y., Qiao, R., Wu, C., He, P., Yin, L., Cheng, R., Wang, F., Wang, Z., et al. (2019). Sub-millimeter-Scale growth of one-unit-cell-thick ferrimagnetic Cr2S3 nanosheets. Nano Lett. *19*, 2154–2161. https://doi.org/10.1021/acs.nanolett.9b00386.

70. Kang, L., Ye, C., Zhao, X., Zhou, X., Hu, J., Li, Q., Liu, D., Das, C.M., Yang, J., Hu, D., et al. (2020). Phase-controllable growth of ultrathin 2D magnetic FeTe crystals. Nat. Commun. *11*, 3729. https://doi.org/10.1038/s41467-020-17253-x.

71. Zheng, H., Huang, C., Lin, F., Fan, J., Liu, H., Zhang, L., Ma, C., Wang, C., Zhu, Y., and Yang, H. (2023). Two-dimensional van der Waals ferromagnetic thin film CrTe2 with high Curie temperature and metallic conductivity. Appl. Phys. Lett. *122*, 023103. https://doi.org/10.1063/5.0130479.

72. Mak, K.F., Shan, J., and Ralph, D.C. (2019). Probing and controlling magnetic states in 2D layered magnetic materials. Nat. Rev. Phys. *1*, 646–661. https://doi.org/10.1038/s42254-019-0110-y.

73. Sato, K. (1981). Measurement of magneto-optical Kerr effect using piezo-birefringent modulator. Jpn. J. Appl. Phys. *20*, 2403.

74. Yamamoto, S., and Matsuda, I. (2017). Measurement of the resonant magneto-optical Kerr effect using a free electron laser. Appl. Sci. *7*, 662. https://doi.org/10.3390/app7070662.

75. Klein, D.R., MacNeill, D., Lado, J.L., Soriano, D., Navarro-Moratalla, E., Watanabe, K., Taniguchi, T., Manni, S., Canfield, P., Fernández-Rossier, J., and Jarillo-Herrero, P. (2018). Probing magnetism in 2D van der Waals crystalline insulators via electron tunneling. Science *360*, 1218–1222. https://doi.org/10.1126/science.aar3617.

76. Adeyeye, A.O., and Shimon, G. (2015). Chapter 1 - growth and characterization of magnetic thin film and nanostructures. In Handbook of Surface Science, R.E. Camley, Z. Celinski, and R.L. Stamps, eds. (North-Holland), pp. 1–41. https://doi.org/10.1016/B978-0-444-62634-9.00001-1.

77. Braginski, A.I., and Clarke, J. (2004). Introduction. In The SQUID Handbook, pp. 1–28. https://doi.org/10.1002/3527603646.ch1.

78. Liu, P., Zhu, H., Wu, Q., Lu, Y., and Pu, Y. (2022). Unconventional magneto-transport properties of the layered antiferromagnet Fe1/3NbS2. Appl. Phys. Lett. *121*, 081901. https://doi.org/10.1063/5.0098797.

79. Sürgers, C., Kittler, W., Wolf, T., and Löhneysen, H.v. (2016). Anomalous Hall effect in the noncollinear antiferromagnet Mn5Si3. AIP Adv. *6*, 055604. https://doi.org/10.1063/1.4943759.

80. Ikhlas, M., Tomita, T., Koretsune, T., Suzuki, M.-T., Nishio-Hamane, D., Arita, R., Otani, Y., and Nakatsuji, S. (2017). Large anomalous Nernst effect at room temperature in a chiral antiferromagnet. Nat. Phys. *13*, 1085–1090. https://doi.org/10.1038/nphys4181.

81. Nayak, A.K., Fischer, J.E., Sun, Y., Yan, B., Karel, J., Komarek, A.C., Shekhar, C., Kumar, N., Schnelle, W., Kübler, J., et al. (2016). Large anomalous Hall effect driven by a nonvanishing Berry curvature in the noncolinear antiferromagnet Mn3Ge. Sci. Adv. *2*, e1501870. https://doi.org/10.1126/sciadv.1501870.

82. Zhou, J., Zhang, W., Lin, Y.-C., Cao, J., Zhou, Y., Jiang, W., Du, H., Tang, B., Shi, J., Jiang, B., et al. (2022). Heterodimensional superlattice with in-plane anomalous Hall effect. Nature *609*, 46–51. https://doi.org/10.1038/s41586-022-05031-2.

83. Thomson, W., XIX (1987). On the electro-dynamic qualities of metals:—effects of magnetization on the electric conductivity of nickel and of iron. Proc. Roy. Soc. Lond. 546–550.

84. Bodnar, S.Y., Šmejkal, L., Turek, I., Jungwirth, T., Gomonay, O., Sinova, J., Sapozhnik, A.A., Elmers, H.J., Kläui, M., and Jourdan, M. (2018). Writing and reading antiferromagnetic Mn2Au by Néel spin-orbit torques and large anisotropic magnetoresistance. Nat. Commun. *9*, 348. https://doi.org/10.1038/s41467-017-02780-x.

85. Coleman, R.V., and Isin, A. (1966). Magnetoresistance in iron single crystals. J. Appl. Phys. *37*, 1028–1029. https://doi.org/10.1063/1.1708320.

86. Wang, Z., Gutiérrez-Lezama, I., Ubrig, N., Kroner, M., Gibertini, M., Taniguchi, T., Watanabe, K., Imamoğlu, A., Giannini, E., and Morpurgo, A.F. (2018). Very large tunneling magnetoresistance in layered magnetic semiconductor CrI3. Nat. Commun. *9*, 2516. https://doi.org/10.1038/s41467-018-04953-8.

87. Song, T., Cai, X., Tu, M.W.-Y., Zhang, X., Huang, B., Wilson, N.P., Seyler, K.L., Zhu, L., Taniguchi, T., Watanabe, K., et al. (2018). Giant tunneling magnetoresistance in spin-filter van der Waals heterostructures. Science *360*, 1214–1218. https://doi.org/10.1126/science.aar4851.

88. Pakhira, S., Islam, F., O'Leary, E., Tanatar, M.A., Heitmann, T., Wang, L.-L., Prozorov, R., Kaminski, A., Vaknin, D., and Johnston, D.C. (2022). A-type antiferromagnetic order in semiconducting EuMg2Sb2 single crystals. Phys. Rev. B *106*, 024418. https://doi.org/10.1103/PhysRevB.106.024418.

89. Rijks, T.G.S.M., Lenczowski, S.K.J., Coehoorn, R., and de Jonge, W.J.M. (1997). In-plane and out-of-plane anisotropic magnetoresistance in Ni80Fe20 thin films. Phys. Rev. B *56*, 362–366. https://doi.org/10.1103/PhysRevB.56.362.

90. Thomson, T. (2014). 10 - magnetic properties of metallic thin films. In Metallic Films for Electronic, Optical and Magnetic Applications, K. Barmak and K. Coffey, eds. (Woodhead Publishing), pp. 454–546. https://doi.org/10.1533/9780857096296.2.454.

91. ed, P.R. (2002). Magnetic sensors and magnetometers. Meas. Sci. Technol. *13*, 645. https://doi.org/10.1088/0957-0233/13/4/707.

92. Fagaly, R.L. (2006). Superconducting quantum interference device instruments and applications. Rev. Sci. Instrum. *77*, 101101. https://doi.org/10.1063/1.2354545.

93. Josephson, B.D. (1962). Possible new effects in superconductive tunnelling. Phys. Lett. *1*, 251–253. https://doi.org/10.1016/0031-9163(62)91369-0.

94. Josephson, B.D. (1974). The discovery of tunnelling supercurrents. Rev. Mod. Phys. *46*, 251–254. https://doi.org/10.1103/RevModPhys.46.251.

95. Buchner, M., Höfler, K., Henne, B., Ney, V., and Ney, A. (2018). Tutorial: basic principles, limits of detection, and pitfalls of highly sensitive SQUID magnetometry for nanomagnetism and spintronics. J. Appl. Phys. *124*, 161101. https://doi.org/10.1063/1.5045299.

96. Clarke, J. (1994). Sci. Am. *271*, 46–53.

97. Zhang, L.-Z., He, X.-D., Zhang, A.-L., Xiao, Q.-L., Lu, W.-L., Chen, F., Feng, Z., Cao, S., Zhang, J., and Ge, J.-Y. (2020). Tunable Curie temperature in layered ferromagnetic Cr5+xTe8 single crystals. Apl. Mater. *8*, 031101. https://doi.org/10.1063/1.5143387.

98. Fujisawa, Y., Pardo-Almanza, M., Garland, J., Yamagami, K., Zhu, X., Chen, X., Araki, K., Takeda, T., Kobayashi, M., Takeda, Y., et al. (2020). Tailoring magnetism in self-intercalated Cr1+δTe2 epitaxial films. Phys. Rev. Mater. *4*, 114001. https://doi.org/10.1103/PhysRevMaterials.4.114001.

99. Polesya, S., Mankovsky, S., Benea, D., Ebert, H., and Bensch, W. (2010). Finite-temperature magnetism of CrTe and CrSe. J. Phys. Condens. Matter *22*, 156002. https://doi.org/10.1088/0953-8984/22/15/156002.

100. Hamasaki, T., Hashimoto, T., Yamaguchi, Y., and Watanabe, H. (1975). Neutron diffraction study of Cr2Te3 single crystal. Solid State Commun. *16*, 895–897. https://doi.org/10.1016/0038-1098(75)90888-1.

101. Tang, B., Lu, Y., Zhou, J., Chouhan, T., Wang, H., Golani, P., Xu, M., Xu, Q., Guan, C., and Liu, Z. (2020). Machine learning-guided synthesis of advanced inorganic materials. Mater. Today *41*, 72–80. https://doi.org/10.1016/j.mattod.2020.06.010.

102. Xu, M., Tang, B., Lu, Y., Zhu, C., Lu, Q., Zhu, C., Zheng, L., Zhang, J., Han, N., Fang, W., et al. (2021). Machine learning driven synthesis of few-layered WTe2 with geometrical control. J. Am. Chem. Soc. *143*, 18103–18113. https://doi.org/10.1021/jacs.1c06786.

103. Liu, L., Zemlyanov, D., and Chen, Y.P. (2021). Epitaxial growth of monolayer PdTe2 and patterned PtTe2 by direct tellurization of Pd and Pt surfaces. 2D Mater. *8*, 045033. https://doi.org/10.1088/2053-1583/ac166b.

104. Ling, X., Lee, Y.-H., Lin, Y., Fang, W., Yu, L., Dresselhaus, M.S., and Kong, J. (2014). Role of the seeding promoter in MoS2 growth by chemical vapor deposition. Nano Lett. *14*, 464–472. https://doi.org/10.1021/nl4033704.

105. Andrzejewski, D., Myja, H., Heuken, M., Grundmann, A., Kalisch, H., Vescan, A., Kümmell, T., and Bacher, G. (2019). Scalable large-area p–i–n light-emitting diodes based on WS2 monolayers grown via MOCVD. ACS Photonics *6*, 1832–1839. https://doi.org/10.1021/acsphotonics.9b00311.

106. Cun, H., Macha, M., Kim, H., Liu, K., Zhao, Y., LaGrange, T., Kis, A., and Radenovic, A. (2019). Wafer-scale MOCVD growth of monolayer MoS2 on sapphire and SiO2. Nano Res. *12*, 2646–2652. https://doi.org/10.1007/s12274-019-2502-9.

107. Lee, J., Pak, S., Giraud, P., Lee, Y.-W., Cho, Y., Hong, J., Jang, A.R., Chung, H.-S., Hong, W.-K., Jeong, H.Y., et al. (2017). Thermodynamically stable synthesis of large-scale and highly crystalline transition metal dichalcogenide monolayers and their unipolar n–n heterojunction devices. Adv. Mater. *29*, 1702206. https://doi.org/10.1002/adma.201702206.

108. Li, Y., Duerloo, K.-A.N., Wauson, K., and Reed, E.J. (2016). Structural semiconductor-to-semimetal phase transition in two-dimensional materials induced by electrostatic gating. Nat. Commun. *7*, 10671. https://doi.org/10.1038/ncomms10671.

109. Liu, L., Wu, J., Wu, L., Ye, M., Liu, X., Wang, Q., Hou, S., Lu, P., Sun, L., Zheng, J., et al. (2018). Phase-selective synthesis of 1T′ MoS2 monolayers and heterophase bilayers. Nat. Mater. *17*, 1108–1114. https://doi.org/10.1038/s41563-018-0187-1.

110. Guo, Z., Wei, A., Zhao, Y., Tao, L., Yang, Y., Zheng, Z., Luo, D., Liu, J., and Li, J. (2019). Controllable growth of large-area atomically thin ReS2 films and their thickness-dependent optoelectronic properties. Appl. Phys. Lett. *114*, 153102. https://doi.org/10.1063/1.5087456.

111. Yamaguchi, A., Hirohata, A., and Stadler, B.J.H., eds. (2021). Chapter 6 - promising prospects of novel magnetism. In Nanomagnetic Materials (Elsevier), pp. 425–471. https://doi.org/10.1016/B978-0-12-822349-9.00012-2.

112. Niu, K., Qiu, G., Wang, C., Li, D., Niu, Y., Li, S., Kang, L., Cai, Y., Han, M., and Lin, J. (2022). Self-intercalated magnetic heterostructures in 2D chromium telluride. Adv. Funct. Mater. *33*, 2208528. https://doi.org/10.1002/adfm.202208528.